STRAIN INDUCTION ON GE NANOBEAMS BY ELECTROSTATIC ACTUATION

A THESIS SUBMITTED TO
THE GRADUATE SCHOOL OF NATURAL AND APPLIED SCIENCES
OF
MIDDLE EAST TECHNICAL UNIVERSITY

BY

ARMAN AYAN

IN PARTIAL FULFILLMENT OF THE REQUIREMENTS
FOR
THE DEGREE OF MASTER OF SCIENCE
IN
ELECTRICAL AND ELECTRONICS ENGINEERING

SEPTEMBER 2018

Approval of the thesis:

STRAIN INDUCTION AND TUNING ON GE NANOBEAMS BY ELECTROSTATIC ACTUATION

submitted by **ARMAN AYAN** in partial fulfillment of the requirements for the degree of **Master of Science in Electrical-Electronics Engineering Department, Middle East Technical University** by,

Prof. Dr. Halil Kalıpçılar   _____
Dean, Graduate School of **Natural and Applied Sciences**

Prof. Dr. Tolga Çiloğlu   _____
Head of Department, **Electrical and Electronics Engineering**

Asst. Prof. Dr. Selçuk Yerci   _____
Advisor, **Electrical and Electronics Engineering, METU**

Examining Committee Members:

Prof. Dr. Cengiz Beşikci   _____
Electrical and Electronics Engineering, METU

Assist. Prof. Dr. Selçuk Yerci   _____
Electrical and Electronics Engineering, METU

Assoc. Prof. Dr. Barış Bayram   _____
Electrical and Electronics Engineering, METU

Prof. Dr. Hüsnü Emrah Ünalan   _____
Metallurgical and Materials Engineering, METU

Assist. Prof. Dr. Samad Nadimi Bavil Oliaei   _____
Mechanical Engineering., Atilim University

                                               Date: 05.09.2018

I hereby declare that all information in this document has been obtained and presented accordance with academic rules and ethical conduct. I also declare that, as required by these rules and conduct, I have fully cited and referenced all material and results that are not original to this work.

Name, Last name: Arman AYAN

Signature:

ABSTRACT

STRAIN INDUCTION ON GE NANOBEAMS BY ELECTROSTATIC ACTUATION

Ayan, Arman

M.S., Electrical and Electronics Engineering

Supervisor: Asst. Prof. Dr. Selçuk Yerci

September 2018, 85 pages

Germanium (Ge) is one of the most promising materials to accomplish the monolithic integration of optics and electronics on the same chip, mainly due to its compatibility with the existing silicon (Si) technology, high charge carrier mobility and high absorption coefficient in the near-infrared region. However, realization of efficient Ge light emitters requires techniques such as tensile strain induction, tin (Sn) incorporation and/or heavy n-type doping to alter its band gap enabling direct transitions. Among these techniques, low-threshold Ge laser has been demonstrated by strain induction. Yet, an integrated-circuit (IC) compatible method capable of tuning the strain dynamically is yet to be shown. In this thesis, a novel way of inducing strain on Ge nanobeams via electrostatic actuation is proposed, which offers simple fabrication and post-fabrication tunability. Ge nanobeam is modeled by finite element method, and the deflection and strain formation are discussed with inherent non-idealities. The maximum deflection is set to one third of the initial gap ($g/3$) distance between the Ge nanobeam and Si substrate to operate at a safe margin from pull-in.

The effect of the dimensions on the required deflection and voltage to reach a predetermined strain is investigated at g/3 deflection. Moreover, possible electrical and mechanical failure mechanisms are discussed together with possible structural modifications to reduce the required voltages. Lastly, the electrical analysis of the nanobeam structures are analyzed and the results showed that non-uniform strain profile could outperform uniformly strained structures. This thesis shows that the required strain to observe direct band transition of Ge can be achieved via electrostatic actuation of Ge nanobeams. Therefore, the proposed Ge nanobeams could lead to a tunable and IC compatible Ge laser on Si that can serve as the key missing component of the monolithically-integrated chips.

ÖZ

GE NANOKİRİŞLER ÜZERİNE ELEKTRIKSEL HAREKETLENDİRME ILE GERINIM OLUŞUMU

Ayan, Arman

Yüksek Lisans, Elektrik-Elektronik Mühendisliği

Tez Yöneticisi: Dr. Öğr. Üyesi Selçuk Yerci

Eylül 2018, 85 sayfa

Germanyum (Ge), var olan silisyum teknolojisiyle uyumu, yüksek yük taşıyıcı mobilitesi ve yakın kızılötesi bölgesindeki yüksek soğurma katsayısından dolayı elektrik ve optik devrelerin tek parça birleşimini başarmak için ümit veren malzemelerdendir. Fakat Ge'den verimli ışık yayıcılar üretmek için, Ge üzerinde çekme gerinimi oluşumu, Ge'yi kalayla katkılama ve yoğun n-tipi katkılama gibi tekniklerle Ge'nin bant yapısını direkt geçişe uygun şekilde değiştirmek gerektirmektedir. Bu tekniklerin arasında çekme gerinimi uygulanarak düşük eşikli Ge lazer üretimi başarılmıştır. Fakat şu ana kadar entegre devre (ED) üretimi ile uyumlu dinamik olarak çekme genirimini kontrol edebilecek bir method gösterilmemiştir. Bu tezde özgün bir teknik olan Ge nanokirişlerde elektriksel hareketlendirilmeyle gerinim oluşturulması önerilmiştir. Bu teknik aynı zamanda hem üretim basitliği hem de üretim sonrası gerinim kontrolünü sağlamaktadır. Ge nanokirişler yapı sonlu-element-metodu simulasyonları ile modellenmiş ve sapma miktarı ve gerinim oluşumu bünyesel ideal

olmayan etkilerle beraber incelenmiştir. Çökme noktasından yeterli bir mesafede çalışmak için maksimum sapma miktarı, Ge nanokiriş ile Si alttaş arasındaki ilk mesafenin üçte birine eşitlenmiş (g/3) ve Ge nanokirişlerinin boyutlarının belirli gerinim değerine ulaşmak için gereken sapma miktarı ve voltaj üzerindeki etkisi g/3'te incelenmiştir. Dahası, muhtemel elektriksel ve mekanik arıza mekanizmaları ve gereken voltajı düşürmek için olası yapısal değişimlerle incelenmiştir. Son olarak yapıların elektriksel analizi yapılmış ve tekdüze olmayan gerinim profilinin tekdüze gerinim profilli yapıdan daha verimli olabileceği gösterilmiştir. Bu tez, direkt bant yapısına geçiş için gerekli gerinimin elektrostatik hareketlenme ile elde edilebileceğini göstermiştir. Bu sebeple, önerilen Ge nanokirişler, ED uyumlu ve gerinim kontrollü Si üzerinde Ge lazer üretimine öncülük edebilir ve bu lazer tek parça birleşimli çiplerin temel eksik parçası olabilir.

Anahtar kelimeler: Grup IV fotoniği, gerinim oluşturma, germanyum, tek-chip üzerinde lazer , elektostatik hareketlendirme

To my mother

ACKNOWLEDGEMENTS

First, I would like to thank Asst. Prof. Dr. Selçuk Yerci for accepting me to APP research group and guiding me throughout my M.S. studies. He always challenged me to reach my highest potential.

I would also like to thank Deniz Türkay for his extensive contributions in optoelectrical simulations of the structures and in the discussion part of the results.

My gratitude also goes to Asst. Prof. Dr. Çiçek Boztuğ for introducing the initial strain induction idea and Asst. Prof. Dr. Samad Nadimi for his guidance during the establishment of the simulations.

I would like to convey my gratitude to Z. İrem Özyurt and Can Özcan for sharing the most stressful times and being supportive all the time.

I am very thankful to all APP members, especially to Gence Bektaş, Wiria Soltanpour, Wisnu Hadibrata, Hava Z. Kaya, Mehmet Koç and M. Cem Şahiner for their help as group members.

I am also grateful to Buse Ünlü for her help for the initial strain simulations and Parisa Naghinazhadahmadi for coming up with the idea of validating the simulations.

I would like to thank my family, notably my mother, for their moral support during my M.S. studies.

Lastly, I would like to thank Semanur Dogru for her fruitful discussions for the organization of my thesis.

TABLE OF CONTENTS

LIST OF TABLES

LIST OF FIGURES

xvii

NOMENCLATURE

Ge	Germanium
Si	Silicon
Sn	Tin
GOI	Germanium-on-Insulator
GaAs	Gallium-arsenide
GeSn	Germanium-tin
SiO_2	Silicon dioxide
SiN_x	Silicon nitride
IC	Integrated circuit
FEM	Finite-element-method
FEA	Finite-element-analysis
CMOS	Complimentary metal-oxide semiconductor
CVD	Chemical vapor deposition
SDT	Small deflection theory
IR	Infrared
SRH	Schokley-Read-Hall
C	Capacitance
ϵ_o	Permittivity of vacuum
g_0	The initial gap distance
w	Deflection
V	The applied voltage
U_{cap}	Energy stored in the capacitor
U_{bat}	Energy stored in the battery
W_{mech}	Mechanical work
Q	Charge
F_e	Electrical force
p_e	Electrical pressure
F_m	Mechanical restoring force
k_m	Mechanical spring constant

V_{pi}	Pull-in voltage
w_{pi}	Pull-in deflection
L	Length of the structure
t	Thickness of the structure
b	Width (breadth) of the structure
E	Young's Modulus
E_{Ge}	The Young's modulus of germanium
E_{SiO2}	The Young's modulus of silicon dioxide
E_{Si}	The Young's modulus of silicon
ν	Poisson's ratio
ν_{Ge}	The Poisson's ratio of germanium
ν_{SiO2}	The Poisson's ratio of silicon dioxide
ν_{Si}	The Poisson's ratio of silicon
d	Density
d_{Ge}	The density of germanium
d_{SiO2}	The density of silicon dioxide
d_{Si}	The density of silicon
ϵ_{SiO2}	The relative permittivity of silicon dioxide
ϵ_{SiNx}	The relative permittivity of silicon nitride
I	Moment of Inertia
ε	Strain
σ	Stress
G	Shear Modulus
R	Radius of curvature
R_{NP}	The radius of curvature of the neutral plane
E_{BD}	Breakdown electric field
V_{BD}	Breakdown voltage
A	The saturation ionization in the gas
B	Excitation and ionization energy parameter
p	Gas pressure

γ	Townsend's secondary ionization coefficient
$C_{vac,2C}$	The capacitance of the vacuum filled region for the structure without the dielectric layer
$C_{ox,2C}$	The capacitance of the oxide filled region for the structure without the dielectric layer
g_{2C}	The gap distance of the structure without the dielectric layer
$C_{ox,3C}$	The capacitance of the oxide filled region for the structure with the dielectric layer
$C_{d,3C}$	The capacitance of the dielectric layer for the structure with the dielectric layer
$C_{vac,3C}$	The capacitance of the vacuum filled region for the structure with the dielectric layer
g_{3C}	The total gap distance for the structure with the dielectric layer
t_d	Thickness of the dielectric layer
ϵ_d	The relative permittivity of the dielectric layer
g_{eff}	Effective gap distance
σ_{vac}	The charge density formed on vacuum filled capacitance
$E_{z,ox}$	The electric field in the z- direction on the oxide
t_{max}	Maximum possible dielectric thickness
t_N	The thickness of the stressed nitride
L'	The separation of the silicon dioxide layers for the initially strained structre
ε_{bi}	Biaxial tensile strain

CHAPTER 1

INTRODUCTION

After the invention of the first transistor was invented in 1947 at Bell's Laboratory, the IC technology started the information era and led to groundbreaking technological advancements. Miniaturization of transistors lies at the heart of this revolutionary development, which has boosted both the performance and the number of transistors in a chip fulfilling the enormous communication and data storage need that people have today. The transistor count in a microprocessor has increased from thousands to billions since the mid-1900s. Intel's co-founder Gordon Moore claimed that the number of transistors in a chip will double in every 24 months, which is now referred to as Moore's Law, and his claim seems to be right so far [1], [2].

As all exponential growth trends, Moore's Law is bound to come to an end. Faltering started in the 2000s as the growth of clock speeds of the circuits cannot maintain its pace due to excessive heat dissipation [3]. Although the sizes of the transistors recently managed to reach down to 14 nm, it is not expected to get lower than several nm since quantum uncertainties start to dominate in that regime [4].

Numerous technologies are competing to be the successor of the existing CMOS technology [5]. Among them, monolithic integration of optics and electronics on the same chip is one of the most promising candidates to maintain the increasing demand for data processing and communication. The optical interconnects can be a substantial solution for the excessive heat dissipation at high clock speeds and can greatly enhance the data processing capability [6].

Since Si overwhelmingly dominates electronics technology, a material which is both capable of being used in efficient photonic devices and compatible with Si technology is required to implement monolithically integrated optics and electronics.

However, the indirect band structure of Si has been a great handicap. Still, the efforts to pursue Si-based photonic devices still continues by utilizing optical non-linearities, quantum confinement effects, incorporation of other group IV semiconductors and heterogeneous on-chip integration of III-V semiconductors [7]–[9].

1.1. Fundamental Properties of Germanium

Ge element was unknown to people up until the first prediction of the element by Mendeleev and its discovery in the late 1800s. However, the element was considered to be a poorly conducting metal and could not find an area of utilization prior to the cutting-edge invention of the first transistor [10]. After that, the interest in Ge boomed, increasing the annual production from a few hundred kilograms to tens of metric tons in almost a decade [11]. However, once high purity Si was achieved, Ge gave its position as the primary semiconductor of electronics to Si due to silicon's superior oxide quality, better thermal behavior, much lower cost and excessive abundance in Earth's crust. Still, the significance of these disadvantages can be minimized by growing thin single-crystalline Ge layers on Si substrate except for the oxide quality.

Recently, high-κ dielectric technology has been developed to overcome the shortages of silicon dioxide (SiO_2), and utilizing the better carrier mobility of Ge has become attractive again (Table 1.1). Moreover, since Ge is also lattice-matched with gallium arsenide (GaAs), high-quality GaAs films can be epitaxially grown on Ge films. Therefore, Ge p-type and GaAs n-type transistors can replace Si ones to enhance the performance of chips [13].

Table 1.1. Tabulation of elementary properties of common semiconductors [12]

Material / Property	Si	Ge	GaAs
Electron Mobility (cm^2/V-s)	1400	3900	8500
Hole Mobility (cm^2/V-s)	450	1900	400
Lattice Constant (Å)	5.431	5.658	5.653
Bandgap (E$_g$)	1.12	0.66	1.42

Another interesting property of Ge is its band structure. Although the main bandgap of Ge is 0.664 eV and the bottom of the conduction band is located at L valley, its direct band gap is only 0.14 eV higher at room temperature, which corresponds to the optical communication wavelength 1550 nm. Thus, Ge has a high absorption coefficient in the near-infrared region and enables the fabrication of high-performance photodetectors [14], [15].

Along with having high absorption coefficient around the near-infrared region, Ge is also shown to exhibit the Quantum Confined Stark Effect [17] and Franz-Keldysh Effect [18]. Ge electro-absorption light modulators, which can be crucial for the modulation of data in photonic IC's, are demonstrated by utilizing these effects [19]–[22].
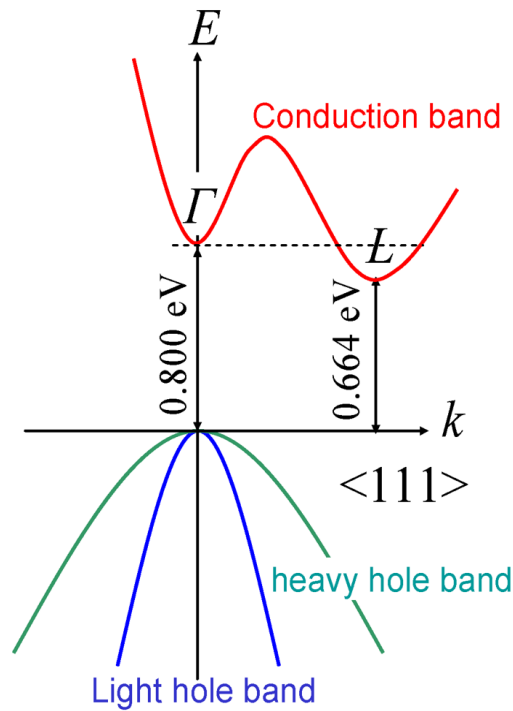
Figure 1.1. The schematic of the band structure of Ge [16]

Although two key elements of integrated electro-optic IC's, i.e. Ge photodetectors and electro-absorption modulators, were fabricated, Ge was doubted to be utilized in integrated electro-optic IC's due to its indirect nature. The electrons at the Γ valley of the Ge's conduction band typically scatters to the L valley before making a radiative recombination, where the non-radiative recombination processes dominate the radiative ones. Thus, achieving efficient bulk Ge light emitters is a great challenge. Lately, however, Ge infrared lasers are fabricated thanks to the band engineering methods, which could be the key missing part of monolithically-integrated Ge electro-optic chips.

1.2. Organization of this dissertation

In this thesis, inducing strain on Ge nanobeams via electrostatic is introduced actuation as depicted in Fig. 1.2, which is an IC-compatible light emission enhancement method is offering post-fabrication tunability. Upon bending of the nanobeam, the strain formation increases the light emission efficiency of Ge, enabling Ge to be used in infrared light emitters. Together with a suitable cavity design, the structure can be utilized in optically pumped lasers. The fabrication of light emitting diode (LED) or electrically pumped lasers requires hole and electron injections to the strained region. A complete electrically pumped light source requires p and n type doping to form homojunction or deposition of materials with different workfunctions for hetorojunction designs.
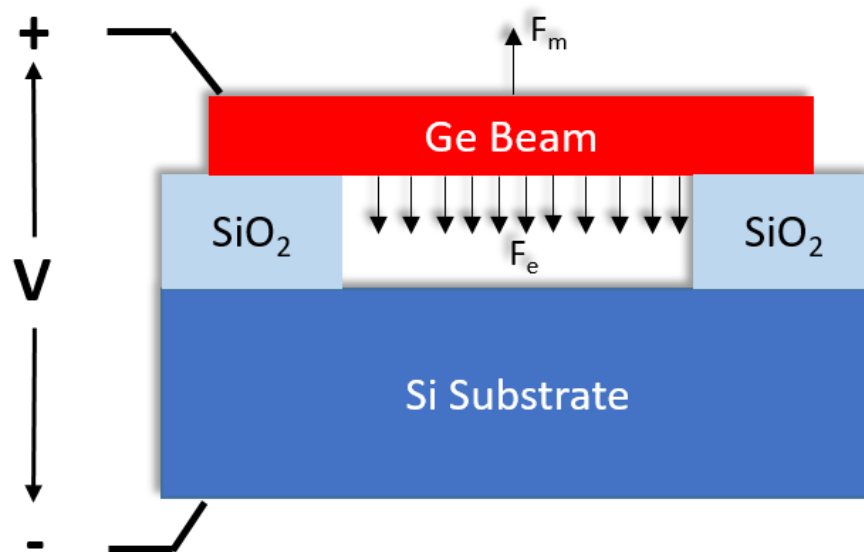
Figure 1.2**.** A cross-section schematic of electrostatically actuated Ge nanobeam for inducing strain.

To analyze the structure in Fig. 1.2, this thesis is divided into the chapters starting with Chapter 1, which provides a brief motivation. In Chapter 2, the common band engineering methods to achieve efficient light emission out of Ge is presented. How strain induction can be used together with other methods is also discussed in this chapter. In Chapter 3, the operation mechanism of electrostatic actuation and how strain can be formed on nanobeams with this method is presented. Chapter 4 covers the strain induction on Ge nanobeams by electrostatic induction. The effect of dimensions and the voltage is investigated with FEM simulations and how they affect the required deflections and voltages to achieve a predetermined strain value is presented together with the comparison to the analytical model. In Chapter 5, the possible failure mechanisms are discussed and a method to overcome electrical failure is presented. Chapter 6 covers alternative structures and modifications that can reduce the required voltage to achieve a predetermined strain. Chapter 7 provides and optoelectrical analysis of strained Ge nanobeams. Finally, the conclusions and future outlook of the Master of Science thesis are given in Chapter 8.

CHAPTER 2

BAND ENGINEERING METHODS TO ENHANCE THE LIGHT EMISSION FROM GERMANIUM

So far three techniques are offered to obtain light emission enhancement from bulk Ge, which are tensile strain induction, n-type doping, and Sn incorporation. In this chapter, these techniques are introduced with a literature survey.

2.1. Tensile Strain Induction

Similar to the most semiconductors, band diagram of Ge gets altered with the induced strain. What is particular to Ge is that the energy difference between bottoms of the conduction bands at Γ and L valleys shrinks with induced tensile strain. Moreover, under sufficient tensile strain, the energetic minimum of Γ valley can even get lower than L valley, turning Ge into a direct bandgap.

The strain formation on Ge can be either biaxial, along two orthogonal crystallographic directions at the equal amount, or uniaxial, only along one crystallographic direction. Direct bandgap Ge can be achieved with both methods yet it requires different amounts of strain. The required tensile strain to achieve direct bandgap is either 1.7 % biaxial tensile strain in the directions orthogonal to the [001] or 4.6 % uniaxial tensile strain along [001] direction [23].

Strain formation on Ge layers is first observed when they are grown on a Si substrate as a result of thermal expansion coefficient mismatch [24]. However, the biaxial tensile strain was much smaller than the expectation which is only around 0.25% [25]. Later, direct bandgap Ge is demonstrated by epitaxial growth on III-V substrates [26], by three-point bending [27], and by deflecting with high-pressure gas

[28]. However, as these techniques are not CMOS friendly, search for different methods to achieve direct bandgap continued. Afterwards, utilization of stressor layers [29]–[34] is widely examined to induce strain on Ge structures.

In 2013, Suess et al. introduced a novel technique to induce strain on Ge which concentrates the strain formed as a result of thermal mismatch to small microbridge, which eventually reached to a uniaxial tensile strain of 5.7% [35], [36]. By utilizing this technique, an optically pumped laser with low threshold power ($3kW/cm^2$) is achieved, which is two orders of magnitude lower than the other state-of-the-art lasers [37].

Together with uniform strain distribution, non-uniform strain distribution is also investigated. The non-uniform strain distribution on Ge forms a pseudo-heterostructure, which is a great advantage to achieve lasing [38]. Since the bottom of the conduction band of strained-Ge lies below that of unstrained one and top of the valence band of strained-Ge lies above that of unstrained one, carriers get confined at the highest strain locations. Carrier confinement enhances the recombination probability and as highest strain locations are the locations where the radiative recombination is maximum, light emission greatly increases. Thus, non-uniform strain based Ge light emitters can offer high quantum efficiencies [39].

2.2. n-type doping

Another approach to compensating 140 meV difference between Γ and L valleys of Ge is n-type doping. The excess electrons in donors fill the states and upon carrier injection higher amount of electrons populate the Γ valley (Fig. 2.1). Moreover, since electrons in the Γ valley deplete faster than the L valley, some of the electrons initially injected into the L valley populate the Γ valley as shown by the dashed line in Fig. 2.1. Therefore, the probability of radiative recombination further increases [16].
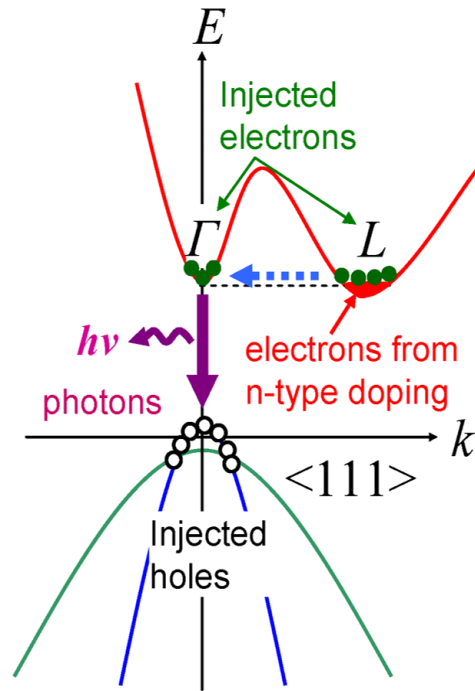
Figure 2.1. The schematic of the band structure of heavily n-type doped Ge layers, and processes occurring upon carrier injection [16]

Heavily n-type doped Ge layers are shown to be capable of being used as a gain medium [25]. However, since the required doping density to achieve efficient light emitters is challengingly high (in the order of 10^{20} cm^{-3}) and growth of Ge on Si inherently causes 0.25% biaxial tensile strain, n-type doping is typically combined with strained Ge. As a result, the required doping level can be reduced down to the order of 10^{19} cm^{-3}.

With a 0.23% tensile strain and the doping concentration of 1×10^{19} cm^{-3}, an optical laser with 50 cm^{-1} gain is reported [40]. With the doping concentration of 4×10^{19} cm^{-3} electrically pumped Ge laser with >400 cm^{-1} is also demonstrated [41]. However, the threshold current density for lasing is around 100 kA/cm^2, which limits the optical power emitted since it causes contact breakdown [29].

Increasing the induced tensile strain or the doping density are the two techniques to increase the gain and to reduce the threshold current density. Although increasing doping density increases the radiative recombination rate, it also increases the non-radiative recombination rate and the free-carrier absorption, which can disrupt lasing [42]. Besides, typical low-solubility and limited activation of the dopants makes it even harder to increase the doping density [43]. Thus, achieving higher tensile strain is preferable.

2.3. Sn Incorporation

Yet another way of modifying the bandgap of Ge is Sn incorporating. Just as in the case of inducing tensile strain, increasing Sn amount in $Ge_{1-x}Sn_x$ compound semiconductor decreases the separation between the bottoms of Γ and L valley. The required Sn percentage to achieve direct bandgap is estimated at 6-8 % of the total volume [44][45].

However, the large lattice mismatch between Ge and α-Sn (14%), the limited equilibrium solubility (1%) of Sn in Ge, and instability of α-Sn over 13ºC hinder the GeSn growth on Ge and Si [46], [47]. Moreover, the growth of GeSn alloy on virtual Ge substrate induces compressive strain on the alloy and further increases the required Sn ratio [45].

Following the advancements in chemical vapor deposition (CVD) growth of GeSn [48]–[50], the aforementioned difficulties are mostly overcome. Direct bandgap GeSn is achieved with around 10% Sn and both photoluminescence and electroluminescence are reported [51]–[53]. Later, GeSn alloys are shown to be utilized as a gain media and GeSn lasing is achieved in 2015 with 12% Sn [54], [55]. Ever since several optically pumped GeSn lasers are demonstrated operating up to 180 K [56]–[58].

10

Although lasing can be also achieved with Sn incorporation, room temperature lasing is yet to be shown. Besides, threshold power for lasing is still remarkably high (>100 kW/cm^2) [55]. Similar to n-type doping, tensile strain induction can be utilized to reduce the threshold power and to reduce the required Sn fraction [45], [52], [59]. Fig. 2.2 shows that instead of utilizing high Sn fraction or high tensile strain, moderate level of Sn and tensile strain can be used to achieve direct band gap. Moreover, the GeSn alloy with 5% Sn fraction and 1% tensile strain provides more gain than the relaxed GeSn alloy with 10% Sn fraction as Fig. 2.3 demonstrates. The combination of tensile strain induction, Sn incorporation, and n-type doping enables a gain of 10^4 cm^{-1} [54].
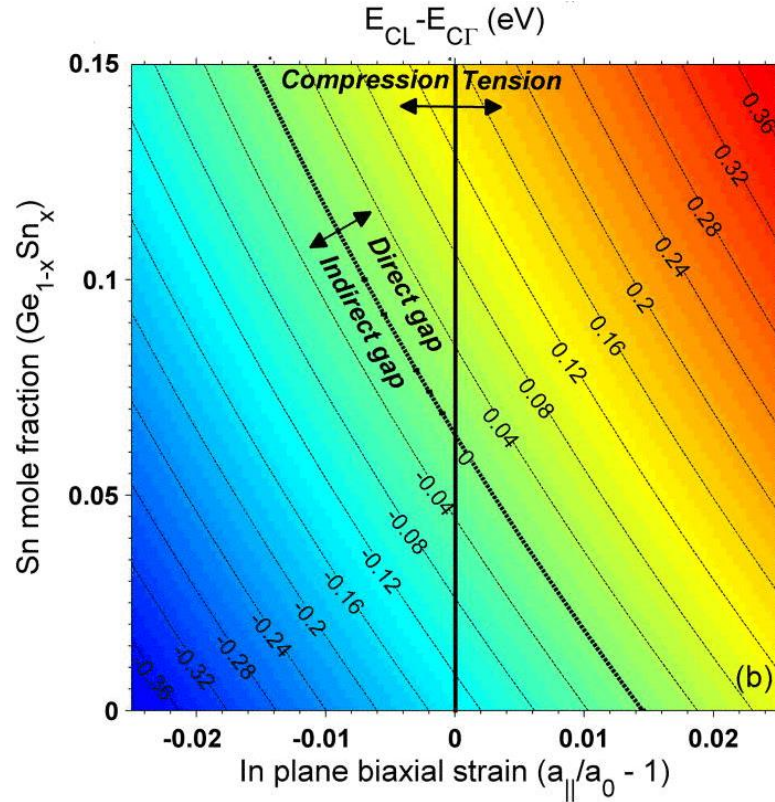
Figure 2.2. The variation of the energy difference between the conduction band minimum at L valley and the conduction band minimum at the Γ valley with Sn mole fraction and biaxial strain [45]

11
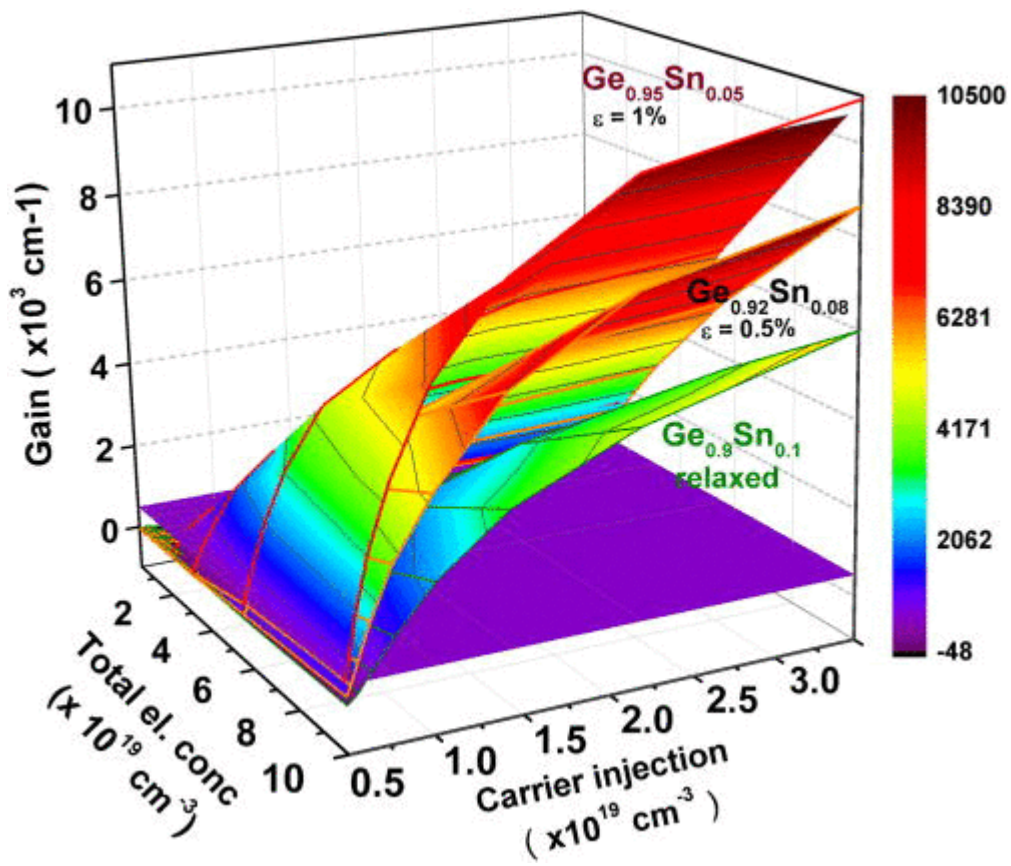
Figure 2.3. The variations of gain with total electron concentration and carrier injection for $Ge_{1-x}Sn_x$ alloys with 0.1 Sn mole fraction and no strain, Sn mole fraction of 0.08 and tensile strain of 0.5% and Sn mole fraction of 0.05 and tensile strain of 1% [54]

CHAPTER 3

STRAIN FORMATION WITH ELECTROSTATIC ACTUATION

In this chapter, the physics of electrostatic actuation is investigated together with the resultant strain formation on nanobeams.

3.1. Electrostatic Actuation

The capacitive structures under applied potential typically experience an electrical force attracting two terminals to each other. The force is especially effective on nanostructures and it can create significant displacement if the structure is suspended.

3.1.1 Operation Principle

Electrostatic actuation can be defined as the electrostatic force formation on a surface to create displacement as a result of applied electrostatic input. Since the formed force is usually a surface force rather than being a volume force, this technique is only useful when the surface-area-to-volume ratio is significantly high, which is typically the case for microstructures and nanostructures. Considering the existing electrical control methods, electrostatic actuation is an appealing candidate for the microactuators [60].

One of the most common forms of the electrostatic actuators is a parallel-plate actuator. This structure is basically a parallel plate capacitor where one of the plates is fixed and the other plate is free to move along the direction of its surface normal, which

is assigned as z-direction, as shown in Fig. 3.1. The capacitance of the parallel plate can be written as

$$C = \frac{\epsilon_0 A}{g_0 - w} \tag{3.1}$$

where ε_0 is the permittivity of the vacuum, A is the surface area of the plate, g_0 is the initial gap distance between the two plates and w denotes the displacement of the movable plate in the z-axis.
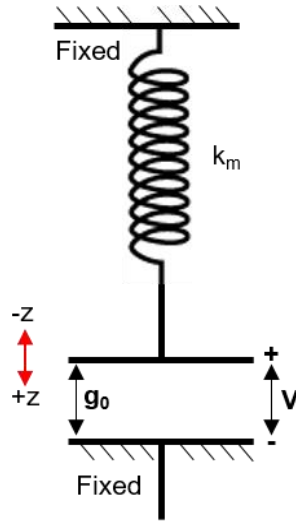
Figure 3.1. The depiction of a parallel plate actuator

The total energy stored in the capacitor, U_{cap}, can be written as

$$U_{cap} = \frac{1}{2}CV^2 = \frac{1}{2}\frac{\epsilon_0 A}{g_0 - w}V^2 \tag{3.2}$$

where V denotes applied electrostatic potential. With the virtual work principle and under the small displacement of Δz, the formed electrostatic force can be found. Since the applied potential between two plates is kept constant rather than the charge on the

structure, the stored energy change on the battery should also be considered in the calculations.

$$\Delta U_{cap} + \Delta U_{bat} = -\Delta W_{mech} \tag{3.3}$$

$$\frac{1}{2}\Delta C V^2 - V \Delta Q = -F_e \Delta w \tag{3.4}$$

where U_{bat} is the stored energy on the battery, W_{mech} is the mechanical work, Q is the total charge and F_e is the magnitude of the electrostatic force. Since the total charge equals to

$$Q = CV \tag{3.5}$$

and the applied potential difference is kept constant, Eq. 3.4 can be written as

$$\frac{1}{2}\Delta C V^2 - V^2 \Delta C = -F_e \Delta w \tag{3.6}$$

$$\frac{1}{2}\Delta C V^2 = F_e \Delta w \tag{3.7}$$

Then the electrostatic force can be found as [61]

$$F_e = \frac{1}{2}\frac{\Delta C}{\Delta w}V^2 = \frac{1}{2}\frac{\delta C}{\delta w}V^2 \tag{3.8}$$

$$F_e = \frac{1}{2}\frac{\delta}{\delta w}\left(\frac{\epsilon_0 A}{g_0 - w}\right)V^2 = \frac{1}{2}\frac{\epsilon_0 A}{(g_0 - w)^2}V^2 \tag{3.9}$$

It is also possible to define electrostatic pressure, which is the electrostatic force per unit area, which equals to

$$p_e = \frac{1}{2}\frac{\epsilon_0}{(g_0 - w)^2}V^2 \tag{3.10}$$

15

Notice that the electrical pressure only depends on the distance between the plates, relative permittivity of the medium, which is assumed to be filled with vacuum, and applied potential difference. The sign of the Eq. 3.10 being positive indicates that the force is actually pulling the movable plate along the +z direction. Moreover, as pressure depends on the square of the applied voltage sign of the bias does not change the direction of the pressure.

With the formation of the electrostatic force, the movable plate starts to accelerate through the fixed plate. However, the movable plate always has a mechanical support to maintain its initial position and that support creates a mechanical restoring force. This restoring force typically modeled with a spring as shown in Fig. 3.1 and obeys the Hooke's Law at the small displacements [60]. Hence, the mechanical restoring force can be written as

$$F_m = -k_m w \qquad (3.11)$$

where F_m denotes the mechanical restoring force and k_m is the mechanical spring constant of the structure. At the equilibrium, the electrostatic force and the mechanical restoring force balance each other at a certain displacement point.

Although the mechanical restoring force acts in the opposite direction of the electrostatic force, its magnitude may not be sufficient to be able to restore the balance. The variation of electrical and mechanical forces at various voltages is shown in Fig. 3.2. At 125 V, around 5 nm and 19 nm deflection, the electrostatic force and mechanical restoring force get equal to each other and equilibrium forms. However, disturbances around 5 and 19 nanometers affects the equilibrium differently. Any change in the position of the movable plate attenuates under the influence of electrostatic and mechanical forces in the former equilibrium, showing that the equilibrium is stable. However, the disturbances in the latter equilibrium get magnified, which either pulls the plate to the stable equilibrium point or collapses the plate to the other terminal, which is, therefore, an unstable equilibrium. As long as the

16

deflection does not exceed the unstable equilibrium point, the equilibrium can be sustained at around 5 nm.

3.1.2 Pull-in
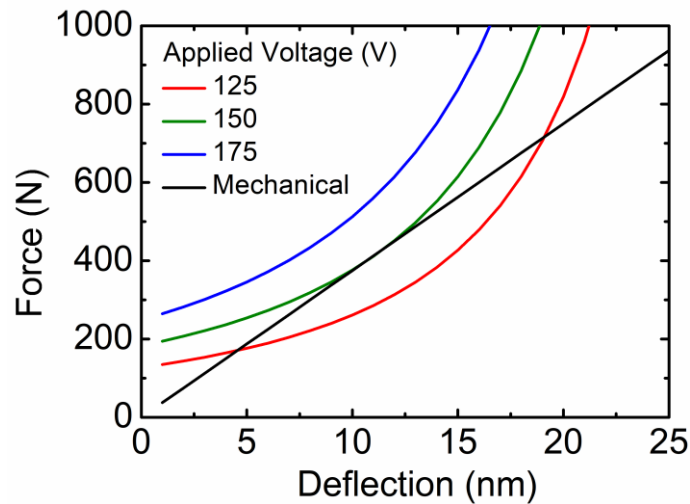
Figure 3.2 Variations of the electrostatic forces under 125, 150 and 175 V together with mechanical restoring force of the structure with a 33 nm gap, 1 mm^2 surface area and a spring constant of 37.5 N/nm.

Although the mechanical restoring force acts in the opposite direction of the electrostatic force, its magnitude may not be sufficient to be able to restore the balance. The variation of electrical and mechanical forces at various voltages is shown in Fig. 3.2. At 125 V, around 5 nm and 19 nm deflection, the electrostatic force and mechanical restoring force get equal to each other and equilibrium forms. However, disturbances around 5 and 19 nanometers affects the equilibrium differently. Any change in the position of the movable plate attenuates under the influence of electrostatic and mechanical forces in the former equilibrium, showing that the equilibrium is stable. However, the disturbances in the latter equilibrium get magnified, which either pulls the plate to the stable equilibrium point or collapses the plate to the other terminal, which is, therefore, an unstable equilibrium. As long as the

17

deflection does not exceed the unstable equilibrium point, the equilibrium can be sustained at around 5 nm.

Even though a stable equilibrium can be established at 125 V, this is not the case when the applied potential is 150 V or higher. The stable and unstable equilibrium points get equal to each other at 150 V and no equilibrium form beyond that voltage and the plate collapses through the other terminal. This phenomenon is commonly known as 'pull-in' and the maximum voltage before pull-in occurs is referred to as 'pull-in voltage'.

The pull-in voltage can be found as equating the deflection derivatives of the magnitudes of the electrostatic force and the mechanical restoring force at the equilibrium point, i.e.

$$\frac{\delta F_e}{\delta w} = \frac{\delta F_m}{\delta w} \tag{3.12}$$

$$k_m = -\frac{\epsilon_0 A}{\left(g_0 - w_{pi}\right)^3}V^2 \tag{3.13}$$

where w_{pi} the maximum deflection before pull-in. Since at the equilibrium point, magnitudes of the electrostatic force and the mechanical restoring force are also equal to each other.

$$|F_m| = |F_e| \tag{3.14}$$

Therefore, Eqs. 3.13 and 3.14 can be combined to find maximum deflection before pull-in.

$$\frac{\epsilon_0 A}{\left(g_0 - w_{pi}\right)^3}V^2 w_{pi} = \frac{1}{2}\frac{\epsilon_0 A}{\left(g_0 - w_{pi}\right)^2}V^2 \tag{3.15}$$

18

$$w_{pi} = \frac{g_0}{3} \qquad (3.16)$$

The maximum deflection, which is known as pull-in distance, is obtained as one-third of the initial gap distance between two terminals. If Eq. 3.14 is combined with the pull-in distance obtained in Eq. 3.16,

$$k_m \frac{g_0}{3} = \frac{1}{2} \frac{\epsilon_0 A}{\left(g_0 - \frac{g_0}{3}\right)^2} V_{pi}^2 \qquad (3.17)$$

$$V_{pi} = \sqrt{\frac{8}{27} \frac{k_m g_0^3}{\epsilon_0 A}} \qquad (3.18)$$

where V_{pi} is the pull-in voltage.

The pull-in distance and voltage obtained in Eqs. 3.16 and 3.18 respectively do not include the fringing fields and non-linearities under the large deflection. The pull-in distance and voltage deviate due to these two effects [60].

Although pull-in might be desirable in certain devices such as capacitive switches, it damages the tunable operation [62] and can create catastrophic results such as short-circuiting, arcing and surface bonding. The short circuit formation can be prevented by insulator deposition on the fixed plate [60]. Moreover, by changing the configuration and control mechanism, the full-gap operation can be achieved [63]–[66].

3.1.3 Electrostatic Actuation of Fixed-Edges Nanobeams

One of the most common structures that are used with electrostatic actuation is the bridge-like nanobeams, which are typically suspended on a dielectric insulator and separated from the other terminal with either a gap of air or vacuum. To characterize

19

this kind of nanobeams, the edges of the beam is typically assumed to be fixed as shown in Fig. 3.3.

Deflection of the fixed-edge nanobeam is much intricate than the piston-like movement of parallel-plate capacitors. The deflection profile is no longer uniform but it is gradually increasing through the center of nanobeam as depicted in Fig. 3.4. Therefore, the force distribution is not uniform as well. Since force distribution and the deflection profile are both coupled to each other, the solutions are typically obtained with numerical iterative methods.
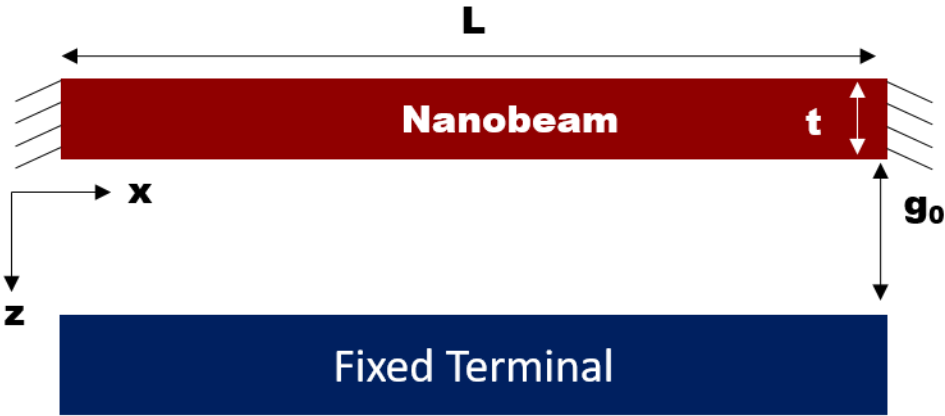
Figure 3.3 2D cross-section schematic of a fixed-edge nanobeam
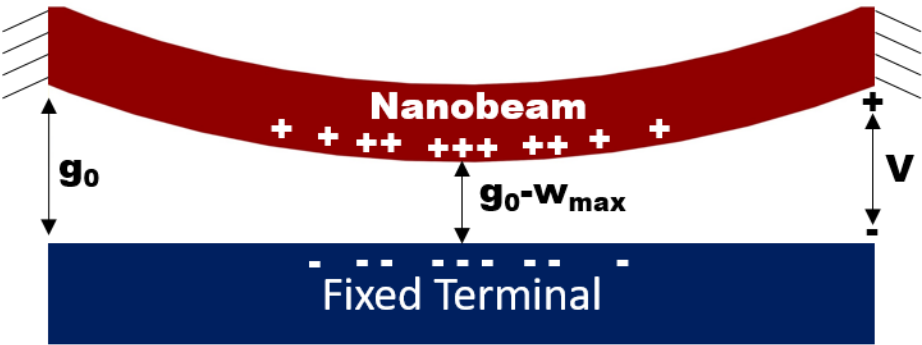
Figure 3.4 Depicted deflection of a fixed-edge nanobeam under the influence of an applied potential

Although there is no direct analytical solution to obtain the deflection profile of the fixed-edges nanobeams, approximate analytical solutions can be obtained. One assumption set to obtain an analytical solution of electrostatic pressure is offered by Chowdhury et al. The assumptions are:

1. The beam is prismatic, i.e. the cross-section of the nanobeam does not change along the beam, and fabricated with a perfectly conducting homogenous material.
2. Before being applied electrostatic potential, the beam is perfectly parallel to the fixed terminal and all six degrees of freedom at the edges are perfectly clamped.
3. The length of the beam is much larger than the breadth and the thickness of the beam so that the beam is within Euler-Bernoulli regime.
4. The stress gradient along the beam is negligible.
5. Any atmospheric loading is neglected.
6. The deflection of the suspended length does not depend on the fringing fields.

Under these assumptions, the electrical pressure is found as

$$p_e = \frac{\epsilon_0 V^2}{2g_0^2} + \frac{0.1325\epsilon_0 V^2}{g_0^{1.25} b^{0.75}} + \frac{0.1265\epsilon_0 t V^2}{g_0^{1.5} b} - \frac{K_{soft-FB,c}}{Lb} \qquad (3.19)$$

where L, t, and b denote the length, thickness, and breadth of the nanobeam, which are the dimensions in x, z, and y, respectively. $K_{soft\text{-}FB,c}$ denotes the spring softening of the fixed-beam with the center deflection [67].

Choi et.al. further neglected the fringing fields and the spring softening effect to be able to obtain an analytical deflection model. The differential equation of the deflection curve can be written as

21

$$EI\frac{\delta^4 w}{dx^4} = p_e = \frac{\epsilon_0 V^2}{\left(g_0 - w(x)\right)^2} \tag{3.20}$$

where E is Young's modulus, $w(x)$ is the deflection profile and I is the moment of inertia which is equal to

$$I = \frac{bt^3}{12} \tag{3.21}$$

Unfortunately, the Eq. 3.20 does not have an analytical solution too. However, if the deflection is assumed to be small enough so that the denominator can be linearized, Eq. 3.20 becomes

$$EI\frac{\delta^4 w}{dx^4} = \frac{\epsilon_0 V^2}{2}(\frac{1}{g_0^2} + \frac{2w}{g_0^3}) \tag{3.22}$$

The differential equation in Eq. 3.22 yields a solution of deflection which is equal to

$$w(x) = \frac{g_0 \sin(l\alpha)\cosh(x\alpha) + g_0 \sinh(l\alpha)\cos(x\alpha)}{2\sin(l\alpha)\cosh(l\alpha) + 2\sinh(l\alpha)\cos(l\alpha)} - \frac{g_0}{2} \tag{3.23}$$

where l is the half-length of the nanobeam and

$$\alpha = \sqrt[4]{\frac{\epsilon_0 V^2 b}{EIg_0^3}} \tag{3.24}$$

To obtain a simpler solution, the term that depends on the deflection can be neglected on the right-hand side of Eq. 3.22 so that it becomes

$$EI\frac{\delta^4 w}{dx^4} = \frac{\epsilon_0 V^2}{2}\frac{1}{g_0^2} \tag{3.25}$$

Then, the solution of the differential equation becomes [68]

$$w(x) = \frac{\epsilon_0 V^2 b}{48EIg^2}(x^2 - l^2)^2 \tag{3.26}$$

And the maximum deflection becomes

$$w(0) = w_{max} = \frac{\epsilon_0 V^2 b}{48EIg^2}l^4 = \frac{\epsilon_0 V^2}{4Et^3 g^2}l^4 = \frac{\epsilon_0 V^2}{64Et^3 g^2}L^4 \tag{3.27}$$

The approximation made in Eq. 3.25 also mean that the force gets higher while the deflection is neglected. Thus, it means that the force distribution on the nanobeam actually equals to the force distribution on the parallel plate actuator. Since the coupling of the force to the deflection is disappeared, the result in Eq. 3.27 can be found with Eq. 3.11 as well. Spring constant of the structure with perfectly fixed edges is found as [69]

$$k_m = \frac{384EI}{L^3} \tag{3.28}$$

Thus, the maximum deflection can be found as

$$\frac{\epsilon_0 AV^2}{g_0^2} = \frac{384EI}{L^3}w_{max} \tag{3.29}$$

where A=bL. Thus, the result obtained in Eq. 3.27 can be obtained with this method as well.

23

Pull-in distance and voltage of the fixed edge nanobeams also deviate from those of parallel-plate actuators. There are various studies to find pull-in voltage in literature [67], [70], [71]. Furthermore, it is shown that the pull-in distance of the fixed beam can actually extend up to 40% of the initial gap distance [70], [72].

3.2. Strain Formation

3.2.1. Fundamentals of Stress and Strain

Strain is basically a measure of the transformation of an object as a result of an external force. A bar stretched, and therefore strained, under the effect of external tension is shown in Fig. 3.5. The strain on the bar is defined as

$$\varepsilon \triangleq \frac{\Delta L}{L} \tag{3.30}$$

where L is the initial length of the bar, ΔL is the stretched part as a result of external force and ε is the strain on the bar. When the strain is positive, it is called tensile strain and when the strain is negative it is called compressive strain.
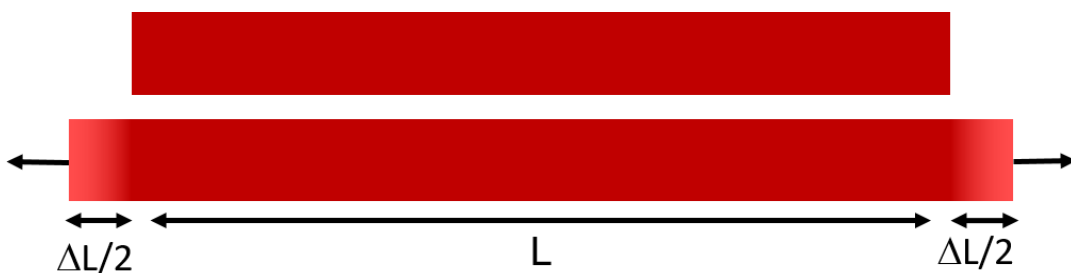
Figure 3.5 Depiction of tensile strain formation on stretched beams

The relation with the force and strain is known as Hooke's Law.

$$\frac{F}{A} = \sigma = E\varepsilon \qquad (3.31)$$

where F is the applied force on the bar, A is the cross-section area of the bar, σ is the stress and E is the Young's Modulus. In reality, Eq. 3.31 is not sufficient to explain the deformation completely since the stretching in one dimension typically causes a shrinkage in the others. Besides, there are also rotational deformations which are called shear strain. Therefore, a more comprehensive model is typically used where stress and strain terms are replaced with 6x1 stress and strain vectors and Young Modulus is replaced with 6x6 tensor. 6 degree of freedom originates from the normal and shear components each having 3 degrees of freedom in all dimensions. This more comprehensive model is known as Generalized Hooke's Law.

The most materials of interest are orthotropic, which means it has three orthogonal planes of symmetry. Therefore, some terms in the stiffness matrix vanish and become

$$
\begin{bmatrix} \varepsilon_1 \\ \varepsilon_2 \\ \varepsilon_3 \\ \varepsilon_4 \\ \varepsilon_5 \\ \varepsilon_6 \end{bmatrix} =
\begin{bmatrix}
\frac{1}{E_1} & -\frac{v_{21}}{E_2} & -\frac{v_{31}}{E_3} & 0 & 0 & 0 \\
-\frac{v_{12}}{E_1} & \frac{1}{E_2} & -\frac{v_{32}}{E_2} & 0 & 0 & 0 \\
-\frac{v_{13}}{E_1} & -\frac{v_{23}}{E_2} & \frac{1}{E_3} & 0 & 0 & 0 \\
0 & 0 & 0 & \frac{1}{2G_{23}} & 0 & 0 \\
0 & 0 & 0 & 0 & \frac{1}{2G_{13}} & 0 \\
0 & 0 & 0 & 0 & 0 & \frac{1}{2G_{12}}
\end{bmatrix}
x
\begin{bmatrix} \sigma_1 \\ \sigma_2 \\ \sigma_3 \\ \sigma_4 \\ \sigma_5 \\ \sigma_6 \end{bmatrix}
\qquad (3.32)
$$

where E_1, E_2, and E_3 are Young's Moduli in 1st, 2nd, and 3rd dimension, ν terms are the Poisson's ratio, the ratio of the transverse strain to the applied strain, of the material with respect to the dimensions shown with the subscript and G terms are Shear Modulus with respect to the dimensions shown with the subscript. When the material is isotropic or its anisotropy is neglected, all Young's Moduli get equal to each other, all Shear Moduli get equal to each other and all Poisson's ratio terms get equal to each other, which further simplify the model [73].

3.2.2. Strain Formation on Deflected Prismatic Beams

Unlike the structure in Fig. 3.5, the structures can also have a stress gradient throughout the structure when there are multiple forces acting on a beam, creating a moment. One of these cases occurs when a transverse load is exerted on a beam with fixed edges. A gradually changing stress and strain forms throughout the beam as the beam deflects as a result of the external transverse load.
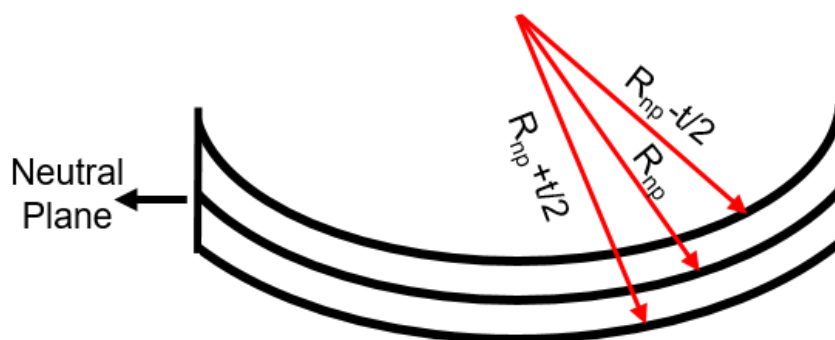
Figure 3.6. The depiction of the deflected beam with the fixed edges and its radius of curvatures at various points

Under the deflection, one surface plane of the beam is under compression and the other surface plane is under tension. Since there is a gradual change from compression to tension, an axis or a plane without any strain form inside the beam, which is called the neutral axis or the neutral plane, respectively. If the beam is prismatic, meaning that its cross-section does not change, homogenous and has a doubly symmetric section,

the neutral plane occurs at the half thickness of the beam as shown in Fig. 3.6. Since the strain on the neutral plane is equal to 0, the strain at any point can be expressed as the change of radius of curvature at that point times infinitesimal angle over the initial length, which is equal to the radius of curvature at the neutral plane multiplied with the infinitesimal angle.

$$\varepsilon(x, y, z) = \frac{Rd\theta - R_{np}d\theta}{R_{np}d\theta} = \frac{\Delta z d\theta}{R_{np}d\theta} = \frac{\Delta z}{R_{np}} \tag{3.33}$$

where R is the radius of curvature at any point, R_{np} is the radius of curvature at the point on the neutral plane on the same cross-section plane and Δz is the distance of the point to the neutral plane in the z-axis. The stress on the beam can be calculated using Hooke's Law and Eq. 3.33. The maximum strain occurs when Δz equals to half thickness and radius of curvature is minimum, which occurs at the upper surface at the fixed edges and the lower surface at the center of the beam. Since the first derivative of the deflection at these positions is 0, the radius of curvature becomes equal to the inverse of the second derivative of the deflection and Eq 3.33 becomes

$$\varepsilon\left(x, y, \frac{t}{2}\right) = \frac{t}{2}\frac{\delta^2 w}{\delta x^2} \tag{3.34}$$

If the deflection profile given in Eq. 3.26, which is the fourth order polynomial deflection profile obtained under the uniformly distributed load, is combined with the Eq. 3.34, the strain becomes

$$\varepsilon\left(0, y, -\frac{t}{2}\right) = \frac{t}{2}\frac{\delta^2}{\delta x^2}\left(w_{max}\left(\left(\frac{x}{l}\right)^2 - 1\right)^2\right) = \frac{4w_{max}}{l^2}\frac{t}{2} = 8\frac{tw_{max}}{L^2} \tag{3.35}$$

$$\varepsilon\left(\pm l, y, \frac{t}{2}\right) = \frac{t}{2}\frac{\delta^2}{\delta x^2}\left(w_{max}\left(\left(\frac{x}{l}\right)^2 - 1\right)^2\right) = \frac{8w_{max}}{l^2}\frac{t}{2} = 16\frac{tw_{max}}{L^2} \tag{3.36}$$

3.2.3. Nonlinear Effects in Deflected Beams

The model explained in 3.2.2 actually requires one of the edges of the nanobeam to move freely in the axial direction. When the edges are completely fixed, an axial force also forms and stretches the beam. As a result, a certain amount of additional, and almost uniform, tensile strain forms on the beam. Therefore, the neutral axis moves along the axis opposite to the deflection and can even vanish as the deflection further increases. The transition roughly occurs when the deflection equals to half thickness and beyond that stretching starts to dominate [74].

As the stretching of the beam increases, it gets harder to further deflect the beam. This phenomenon is known as 'stress stiffening". Similar to fibers in tension, the stiffness of the beam increases. Since the tension forms with the deflection of the beam, stress stiffening can be modeled with non-linear spring constant. Moreover, as pull-in is calculated in section 3.1.2 with linear spring constant, stress stiffening also increases the pull-in distance (from 0.4 to 0.6) and voltage [64]

CHAPTER 4

STRAIN INDUCTION ON GERMANIUM NANOBEAMS VIA ELECTROSTATIC ACTUATION

4.1. Introduction

In this chapter, strain formation upon electrostatic actuation on prismatic suspended Ge nanobeams, which is supported with SiO_2 from both edges is investigated. A schematic of an exemplary Ge nanobeam is depicted in Fig. 4.1a. The length of the suspended region of the nanobeam is denoted as L, the thickness of the nanobeam is defined as t and width (breadth) of the nanobeam is denoted as b. When an electrostatic potential is applied between the Ge nanobeam and Si substrate, the deflection of the nanobeam (Fig. 4.1b) induces strain on Ge and enhancing the light emission. The applied voltage is denoted as V and the gap distance between the two terminals is denoted as g, which is initially constant and equals to g_0.

For the investigation of the structure, finite element analysis (FEA) is utilized and the results are compared to the analytical approximations obtained under certain assumptions. The nanobeams typically have much larger length than the thickness (>5). However, to save the computational power and to be able to explain the trends without the interference of the effect of the changing width, the width is set to infinity with the plane strain assumption, enabling us to reduce the simulation dimensions to 2D. In Section 4.2.4, how width affects the system is discussed and the validity of the 2D simulations is confirmed. Hence, the trends and achieved strain values under the certain voltage are also valid for nanoplate structures.

In the analytic expressions, the origin of the Cartesian system is taken as the midpoint of the nanobeam in x, y and z directions. The nanobeam is symmetric in xz and yz planes, which are the symmetry planes. The intersection of the symmetry planes is referred to as centerline whose midpoint is the origin point. The end of the Ge nanobeam along the center line in the minus z-direction is called as the bottom center of the nanobeam.
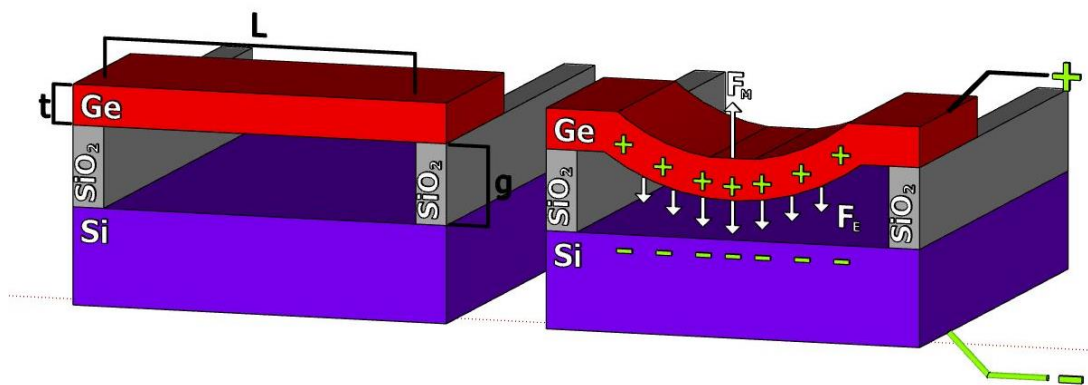
Figure 4.1. Cross-sectional schematics of Ge nanobeam suspended from both sides by SiO_2, (a) before and (b) after the applied voltage.

4.1.1 Meshing and material parameters

In the simulations, the minimum mesh sizes in the nanobeam are set to one-sixth of Ge thickness and the smallest mesh sizes in the oxide region and vacuum region is set to one-sixth of the gap distance. Simulations with triangular and rectangular meshing are also utilized and the simulations with both meshings are in agreement. A sample meshing of the structure is shown in Fig. 4.2.
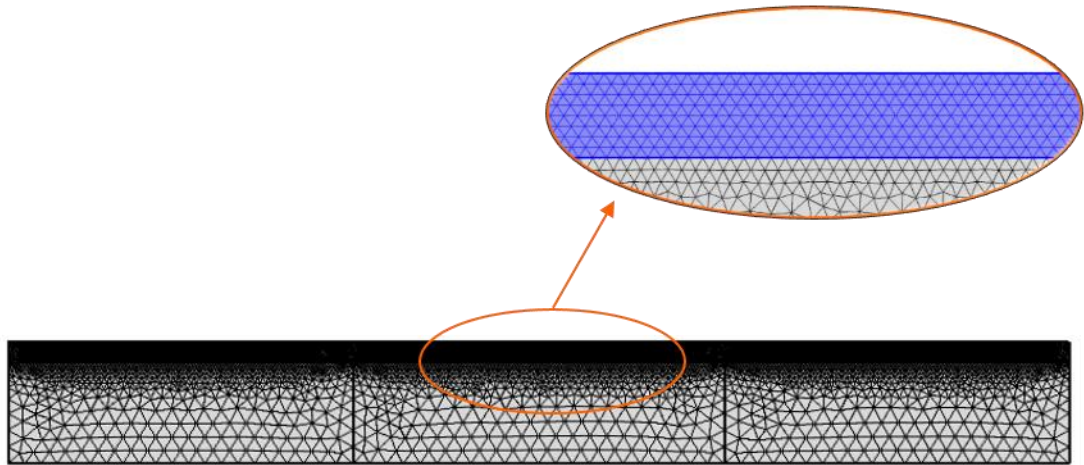
Figure. 4.2 A schematic of the mesh sizes utilized in a typical simulation. The densely meshed region is the Ge nanobeam, the regions at the right and the left bottom are SiO_2 layers and the lower center region is the gap filled with vacuum. The elliptical figure at the top-right is a zoomed schematic to the Ge nanobeam. Ge is highlighted in blue.

The material properties used in the simulations are tabulated in Table. 4.1. Among these properties, the Young's modulus of the nanobeam is particularly important since it directly affects the required voltages. Since Sn incorporation in Ge can reduce the Young's modulus of Ge [75], the required voltages can be slightly smaller for GeSn nanobeams.

Table 4.1. The Young's moduli, Poisson's ratios, densities and the relative permittivity values of the materials of interest.

Parameter	Value	Parameter	Value
E_{Ge} (GPa)	103	d_{Ge} (kg/m^3)	5323
E_{SiO2} (GPa)	70	d_{SiO2} (kg/m^3)	2200
E_{Si} (GPa)	170	d_{Si} (kg/m^3)	2329
ν_{Ge}	0.26	ε_{SiO2}	3.9
ν_{SiO2}	0.17	ε_{Si3N4}	7.5
ν_{Si}	0.28		

4.1.2 Agreement with the Literature

To check the reliability of the simulations, the analytical equations given in the study of the Choi et al.[68] are regenerated by analyzing the beam which is fixed at the two edges under small deflections. In their study, when deflection is significantly lower than the gap, the deflection profile is found as given in Eq.3. 26.

For the L = 2 μm, g = 100nm, t = 30 nm V = 10 V and E=103 GPa, the fixed-fixed case is simulated and the results are found to be in good agreement with the analytic solutions as it is shown in Fig. 4.3.
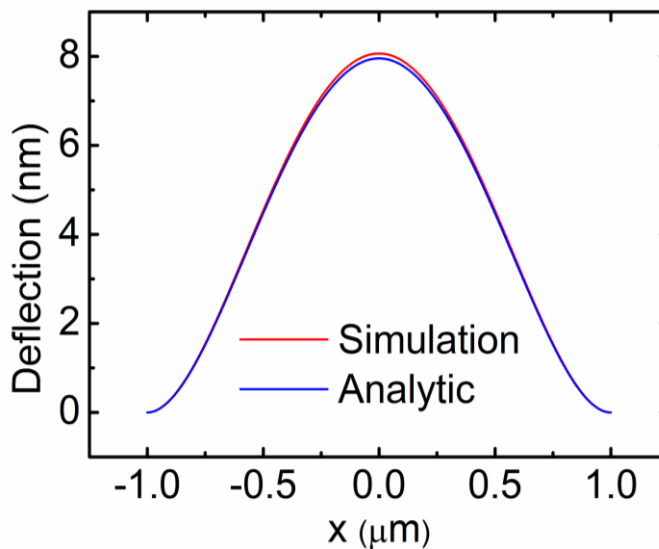
Figure 4.3 The deflection profile along the nanobeam simulated by FEM and analytically calculated using Eq. 3.26. The length and thickness of the Ge nanobeam are 2 μm and 30 nm, respectively. The applied voltage is 10 V. The gap between the Ge nanobeam and Si substrate is 100 nm.

4.1.3 Strain Formation

As the nanobeam bends with the applied voltage, an axial strain (ε) is formed on it as shown in Fig. 4.4. In agreement with the theory provided in Chapter 3, compressive strain forms at the opposite portion of the nanobeam with respect to tensilely strained regions. Although the non-uniform strain profile seems to be a

disadvantage as it reduces the active region of illumination, it can also operate as a comparably efficient light emitting structure thanks to the high carrier localization to the high tensile strain points.

Local maxima of the axial tensile strain occur on the lower portion of the nanobeam at the yz symmetry plane, which is referred to as center plane, and on the upper portion of the nanobeam at the two edges. However, unlike the structures shown in Fig. 4.4, the corners typically get rounded depending on fabrication parameters which can remarkably alter the strain percentage at the edges as discussed in Section 4.4. Hence, only the axial tensile strain around the bottom center of the nanobeam is at the focus of this study. Moreover, even though the deflection profile is not uniform and it gradually increases through the center, the maximum deflection is the most crucial term to determine the strain on the beam.
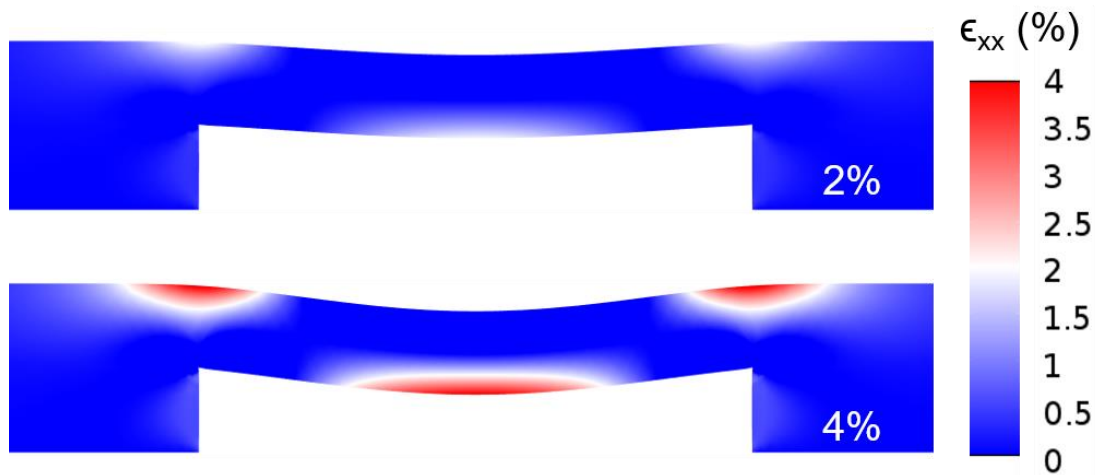
Figure 4.4 Tensile strain profiles of Ge nanobeams for maximum axial strains of 2% and 4% at the bottom center of the nanobeam.

4.2. Effect of Dimensions and Applied Voltage

In the design of strained-Ge nanobeams, the crucial question is how much voltage is required to achieve a predetermined strain value for given dimensions of the nanobeam. Moreover, the dimensions of the nanobeam can be altered to achieve the minimum required voltage. A theoretical approximation can be obtained using Small-Deflection-Theory (SDT) introduced in Chapter 3. By combining Eqs. 3.21, 3.29 and 3.35, the maximum deflection and the strain at the lower portion of the center plane can be expressed as

$$w_{max} = \frac{1}{64} \frac{\epsilon_0}{E} \frac{L^4}{t^3} \frac{V^2}{g^2} \tag{4.1}$$

$$\epsilon_{xx}\left(0, \frac{t}{2}\right) = \frac{1}{8} \frac{\epsilon_0}{E} \frac{L^2}{t^2} \frac{V^2}{g^2} \tag{4.2}$$

where ϵ_{xx} (0,t/2) is the tensile strain at the bottom center of the nanobeam, E_{Ge} is the Young's Modulus of Ge, ϵ_0 is the permittivity of the vacuum and V is the applied voltage. However, SDT is not sufficient to explain the trends since both deflection and strain values are significantly high. Therefore, by utilizing FEM simulations, the trends are presented in this section.

4.2.1 Effect of the Gap Distance and Applied Voltage

The external control parameter of the system is the applied voltage between two terminals. Therefore, how strain changes with the applied voltage is particularly important for tunability. The change of the axial strain and deflection at the bottom of the center plane with increasing applied voltage for three different gap values are presented in Fig. 4.5a and 4.5b, respectively.
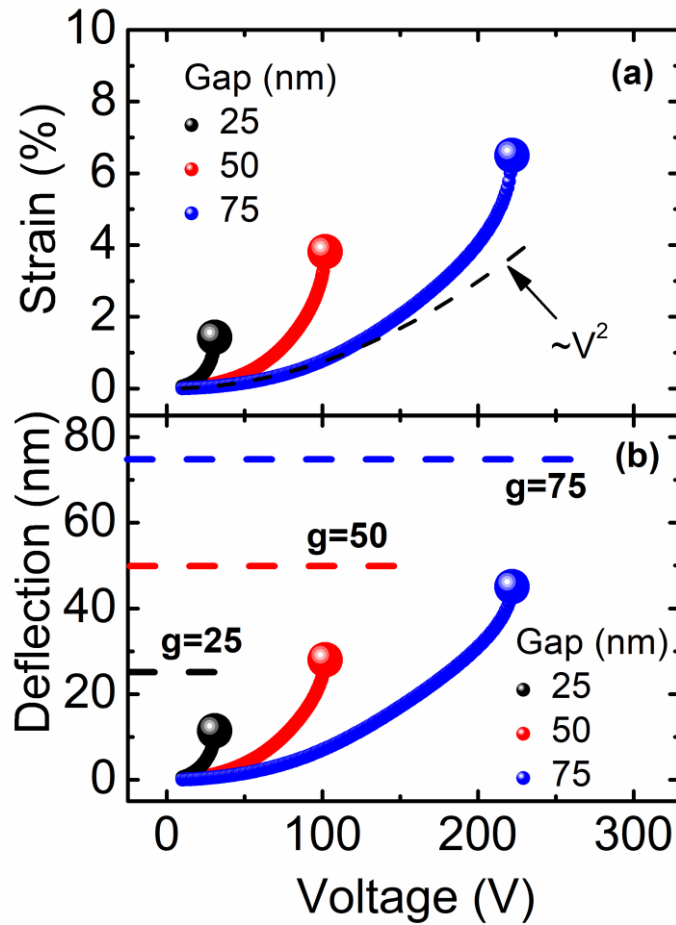
Figure 4.5 Variations of the deflection (a) and the axial strain (b) of the nanobeam at its center of the lower portion with changing voltage for initial gap distances of 25, 50 and 75 nm. The big spheres represent the pull-in point. The square of the applied voltage trend for 75 nm of gap distance is shown with the dashed line.

The Eqs. 4.1 and 4.2 predict a linear increase in both deflection and strain with the square of the applied voltage. However, this prediction deviates from the actual values at high deflections with respect to the gap, as shown in Fig. 4.5a. This is because the increasing potential also causes shrinkage in the gap distance causing a superlinear increase with the square of the applied voltage. At 200 V and 75 nm gap distance, the achieved tensile strain is 1% higher than the expected 3% tensile strain.

As the gap distances increase, the achieved strain at the same voltage decreases as expected. Higher gap distances reduce the electrical force on the nanobeam; and therefore, the achieved strain. However, operating at a lower gap distance limit the

maximum achievable strain value before pull-in occurs. At 25 nm gap, for instance, the maximum achievable strain is even lower than 1.5% tensile strain. Therefore, to be able to reach higher strain values before pull-in occurs, the higher gap values should be used, which significantly increases the required voltage. At 50 nm of gap distance, 3.8% tensile strain can be achieved at the verge of pull-in around 100 V. However, the pull-in point exhibits instability in reality and nanobeams have the possibility of collapsing to the Si substrate even before pull-in. Therefore, the nanobeams are set to operate at a fair margin from pull-in point to provide stability and extend the tunability range of the strain formed. Considering that the pull-in distances of the nanobeams can range from 40% to 60% of the initial gap distance under the effect of stress stiffening, the distance of operation is set to 33% of the initial gap distance ($w=g_0/3$) to operate a fair margin to the smallest pull-in distance. At 50 nm of gap distance, the $w=g_0/3$ condition is satisfied at 89.5 V, which is roughly 90% of the pull-in voltage and allows a tunability range of 1.8% of tensile strain. At this condition, 1.02%, 2.04% and 3.14% tensile strains are achieved at 25, 50 and 75 nm gap distances with corresponding applied voltages of 30, 89.5 and 181 V, respectively. Therefore, by adjusting the gap distances, the various predetermined strain values can be achieved under this condition although the required voltages increase superlinearly. The required deflection (which is 1/3 of the required gap value), and the required voltage can be predicted by SDT as

$$w_{max} = \frac{L^2 \epsilon_{xx}\left(0, \frac{t}{2}\right)}{8t} \tag{4.3}$$

$$V = \frac{3\sqrt{2}}{4} L \sqrt{\frac{E_{Ge}}{\epsilon_0}} \left(\epsilon_{xx}\left(0, \frac{t}{2}\right)\right)^{1.5} \tag{4.4}$$

In the following sections, the $w=g_0/3$ condition will be used frequently to define the gap distance and to operate at the margin. However, it should be noted that less conservative conditions can be utilized to reduce the required voltage, especially at high pull-in distances.

4.2.2 Effect of the Nanobeam Thickness

One of the crucial parameters in the design of a Ge nanobeam is its thickness. In Fig 4.6a and 4.6b, a 2D color graph of the required deflections and voltages to achieve predetermined strain values for different thicknesses, from 7 nm to 70 nm, are shown at 350 nm of beam length under the $w=g_0/3$ condition, respectively. The required deflections exhibit a linear increase on the right-hand side of the dashed line which is in agreement with the SDT. However, as the deflections exceed the half thickness of the nanobeam (shown with the dashed line), the trend becomes sublinear since geometric nonlinearities dominate, which will be discussed in Section 4.3.2. Similarly, the decreasing trend of the required voltage with the decreasing thickness at a constant strain comes to an end around the dashed line makes a local minimum and even start to increase as a result of geometric nonlinearities. However, the geometric nonlinearities do not remarkably affect the increase in required voltage with the strain to the power 1.5, which approximately holds throughout the Fig. 4.6b. The minimum required voltages are roughly obtained for the thickness/length ratios between 0.06 and 0.07, which corresponds to 20-25 nm of thicknesses at 350 nm nanobeam length.
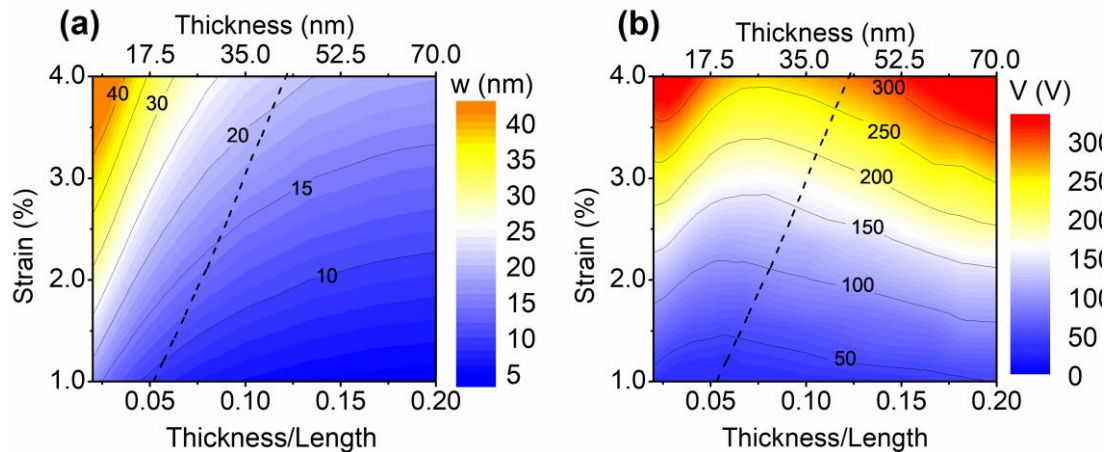
Figure 4.6. The deflection (a) and the applied voltage (b) for various axial strains and t/L ratios. The length of the nanobeam is set to 350 nm. The distance between the Ge nanobeam and Si substrate is equal to 3 times of the deflection shown in (a). The dashed line indicates t=2w.

The required deflection and voltage values are typically higher than Eqs. 4.3 and 4.6 predict due to the elasticity of SiO_2, which is discussed in Section 4.3.1. The required voltage to achieve 4% tensile strain can be minimized to around 270 V by arranging the thickness over length ratio to the optimum point.

4.2.3 Effect of the Nanobeam Length

The length of the nanobeam is another crucial parameter that should be adjusted. Eqs. 4.3 and 4.4 both predict linear increase with the nanobeam length in the deflection and strain provided that the thickness/length ratio is constant. Since the gap is also set to 3 times of the required deflection and since the thickness/length ratio is kept constant, all the dimensions are scaled with the length. Therefore, the required deflection and voltage is also scaled with the length. In Fig. 4.7a and 4.7b, the change of required deflections and voltages to reach 2% tensile strain with the nanobeam length for various thickness/length ratios are shown. The scalability is visible in the simulations. Moreover, the minimum required voltages obtained around 20/350 thickness/length ratio is in agreement with the results obtained in Fig. 4.6.

By utilizing the linearities of the required deflection and voltage with the length and Fig 4.6, the required deflection and voltage values to achieve predetermined strains can be roughly found for a wide range of lengths and thicknesses under the $w = g_0/3$ condition. First, the desired strain percentage and thickness/length ratio are determined and the required deflection and voltage values are obtained for these strain and thickness/length ratio from Fig. 4.6. Then the values are scaled with the ratio of length over 350 nm. Finally, the gap distance is multiplied with 3 times of the required deflection.
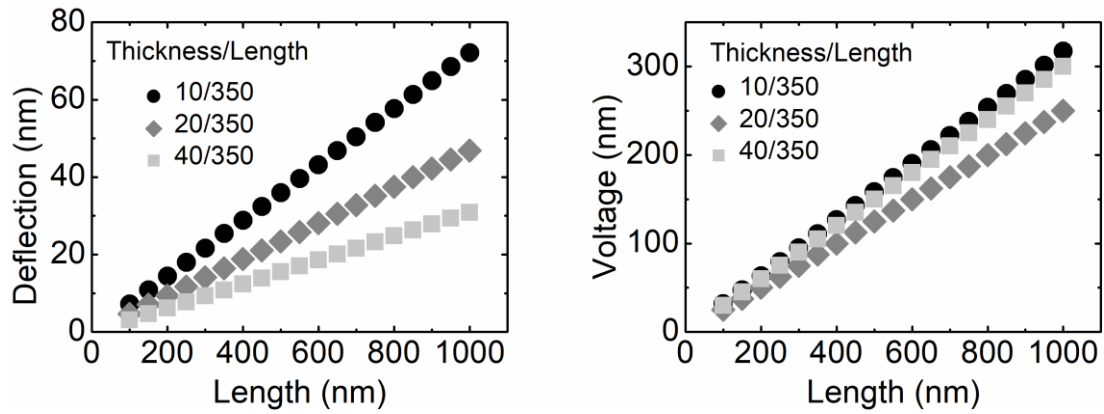
Figure 4.7. The change of the required deflection (a) and voltage (b) to achieve 2% tensile strain with Ge nanobeam length for various t/L ratios under $w=g_0/3$ condition. The length of the nanobeam is 350 nm.

4.2.4 Effect of the Nanobeam Width

The simulations run so far assumed that the width of the beam is much larger than the other dimensions, which is not common for beams. By doing so, simulations are reduced to 2D structures, which saves a great amount of computational power. In this section, the effect of changing width is investigated with 3D simulations together with the comparison of the validity of 2D simulations.

The change of the required voltages to achieve 2% tensile strain with the nanobeam width is shown in Fig. 4.8 at the length of 1000 nm and the thickness/length ratio of 0.05 under the $w=g_0/3$ condition. Clearly, the required voltages decrease as the width of the nanobeam decreases. For relatively narrower nanobeams, electric field lines between the Si substrate and the top and sides of the nanobeam become effective, known as fringing fields. The fringing fields boost the electrical force, and hence; reduce the required voltage. As the width of the beam increases, the effect of the fringing fields become negligible. At width of 25 nm, the required voltage can be reduced up to 35% of the 2D case.

39
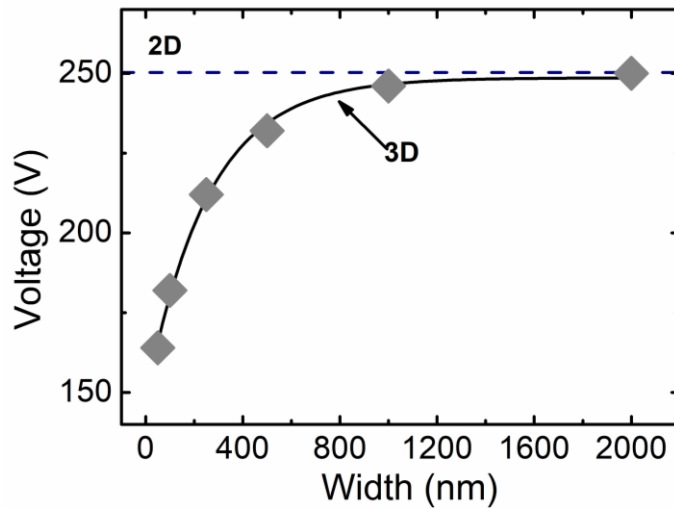
Figure 4.8. The required voltage to achieve 2% tensile strain for various Ge nanobeam widths for a fixed thickness and length of 50 nm and 1 μm, respectively. The solid line is to guide the eye. The dashed line indicates the required voltage to achieve a 2% strain calculated using a 2D model.

The 2D model predicts the required voltage to achieve 2% tensile strain as 250 V, which can be also found approximately by the method offered in Section 4.2.3. As the width of the nanobeam becomes approximately equal to the length of the nanobeam, the 3D simulation results converge to 2D simulations. Therefore, the required voltages found by 2D simulations are valid for wide nanobeams and nanoplates.

4.2.5 Effect of Substrate Thickness

In the simulations, the substrate is removed the save from computation power as its effect is minor. Instead, the interface of the SiO_2 layer with the Si substrate is assumed to be fixed. However, there can be a finite amount of displacement at the interface. The assumption marginally modifies the required voltages.

In Fig. 4.9, the change of the required voltage to achieve 4% tensile strain for a simulation model including a Si substrate and for a simulation model excluding Si. As the thickness of the Si substrate is increased, the change in the required voltage gets smaller and saturates after 1.5 μm substrate thickness. The Si substrate excluded model used in this dissertation slightly overestimates the required voltage (<3%).

40
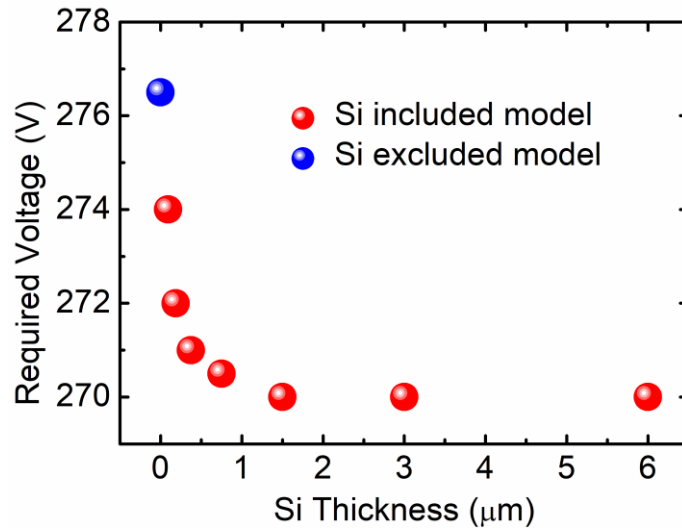
Figure 4.9. The change of the required voltages to achieve 4% tensile strain with increasing Si substrate thickness for the Si substrate included model and for Si excluded model for 350 nm of nanobeam length, 20 nm of thickness and under $w=g_0/3$ condition.

4.3. Discussions of the Non-idealities

As it is discussed throughout the Section 4.2, the required voltages and deflections deviate from the predictions of small deflection theory. The small deflection theory neglects the elasticity of the SiO_2, geometric nonlinearities and the non-uniformity of the electrical force distribution. In this section, how the deflection and strain change is affected with the non-idealities with their physical mechanisms is discussed.

4.3.1 Effect of Elasticity of SiO_2

SDT assumes that the edges are totally clamped and both deflection and its derivative are zero at the edges. However, the edges are actually supported by a SiO_2 layer which has a finite elasticity. Therefore, the SiO_2 layer displaces slightly under the exerted electrical force. Even the slightest displacement at the edges increases the effective length of the beam which increases the required voltage. In Fig. 4.10, the

change of the required deflection and strain with the thickness/length ratio and the tensile strain is shown for 350 nm length and at the fixed edges, which is equivalent to Fig. 4.6 except for that edges are completely fixed. Comparing with Fig. 4.10, both the required deflections and the required voltages are smaller when the edges are fixed for all thickness/length ratios and strain percentages. The elasticity of the SiO_2 layer increases the required deflections and the voltages by approximately 30%. Therefore, the required voltage can be reduced by utilizing insulators with higher Young's moduli or increasing the Young modulus of SiO_2 (~70 GPa).

Once the elasticity of SiO_2 is removed from simulations, the predictions of SDT become more accurate. In Fig. 4.11, the deflection and the strain obtained at various voltages are shown for both fixed edges and for the edges supported by SiO_2. SDT is capable to successfully predict the deflection and voltages achieved at small deflections for the fixed edge nanobeams.
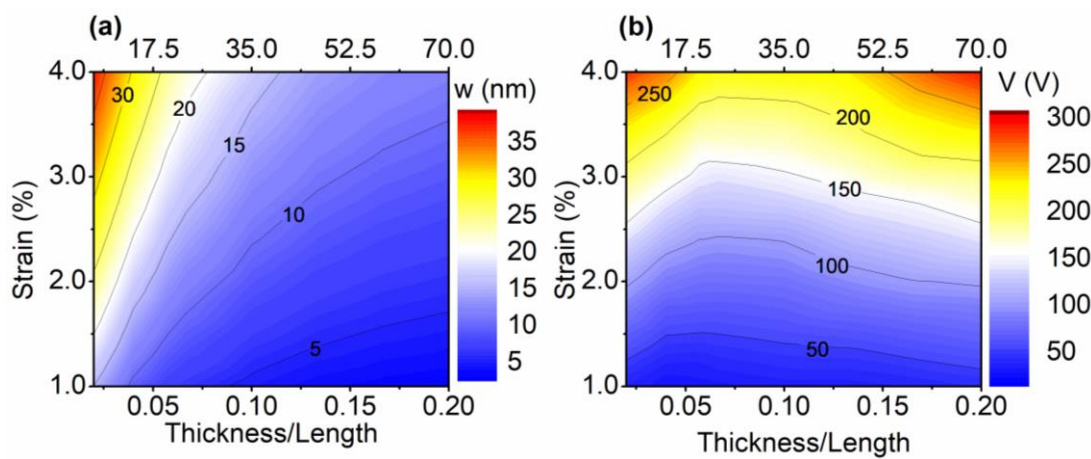
Figure 4.10. (a) The deflection at various axial strains and t/L ratios for fixed edges. The distance between the Ge nanobeam and Si substrate is equal to 3 times the deflection shown in (a). (b) The applied voltage for various axial strains and t/L ratios for fixed edges. The length of the nanobeam is 350 nm in (a) and (b).
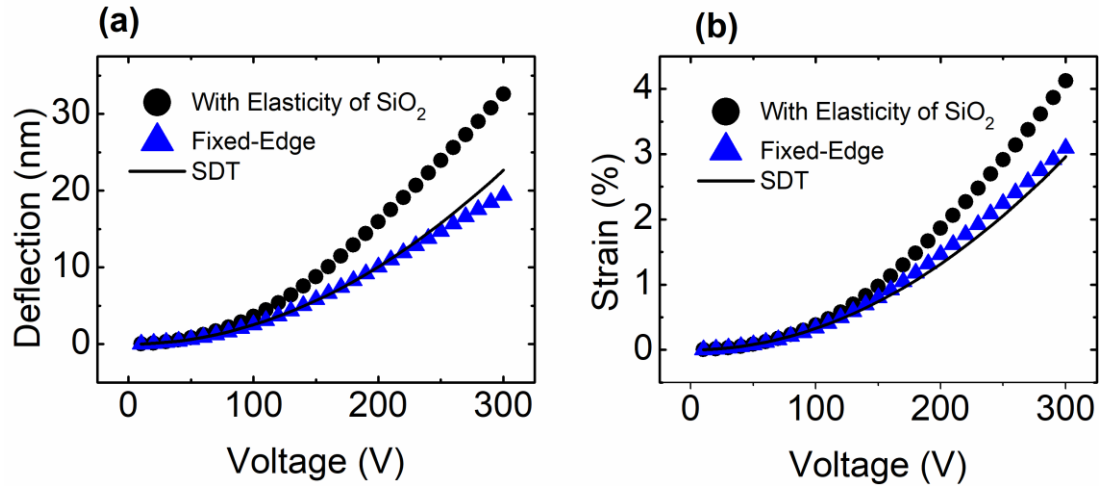
Figure 4.11. (a) The variation of deflection with the applied voltage for the fixed edges and the edges supported by SiO2. (b) The variation of strain with applied voltage for the fixed edges and the edges supported by SiO2. Solid lines in (a) and (b) are relations predicted by the SDT. The length and thickness of the nanobeam are 350 nm and 20 nm, respectively. The gap between the Ge nanobeam and Si substrate is 100 nm.

4.3.2 Geometric Non-linearities

As mentioned in Section 4.2.2, the trends of the required deflections and voltages remarkably change when the deflection exceeds half thickness of the nanobeam since the edges are not free to move in the axial direction. As the nanobeam deflects, an axial force also forms to prevent the nanobeam moving inwards. The axial force causes a tensile strain formation throughout the nanobeam, known as "nonlinear stretching effect". As tensile strain forms, the stiffness of the nanobeam superlinearly increases, referred to as stress stiffening.

The tensile strain formed as a result of stretching is superimposed to the bending-induced strains. Therefore, the predetermined strains are reached at smaller deflections when the stretching is significant. However, this advantage is not translated into the required voltages due to stress stiffening. As the stiffness of the beam increases, the required voltages further increase despite the fact that the required deflections are lower. The change of the required deflections and voltages with the

43

thickness/length ratio and the predetermined tensile strains are shown in Fig. 4.12 for 350 nm of length and ignored nonlinearities, which is which is equivalent to Fig. 4.6 except for that the geometric nonlinearities are ignored. The required deflections and voltages are almost the same as the ones presented in Fig. 4.6 when the deflections are smaller than the half thickness, which is the right-hand side of the dashed line. However, the required deflections are higher and the required voltages are smaller on the right-hand side of the dashed line in Fig. 4.12. The required voltages go down to 180 V to reach 4% tensile strain from 330 V at 0.02 thickness/length ratio when the geometric nonlinearity is ignored. However, in reality, there is no way to get rid of geometric nonlinearities as long as the edges cannot move in the axial direction.
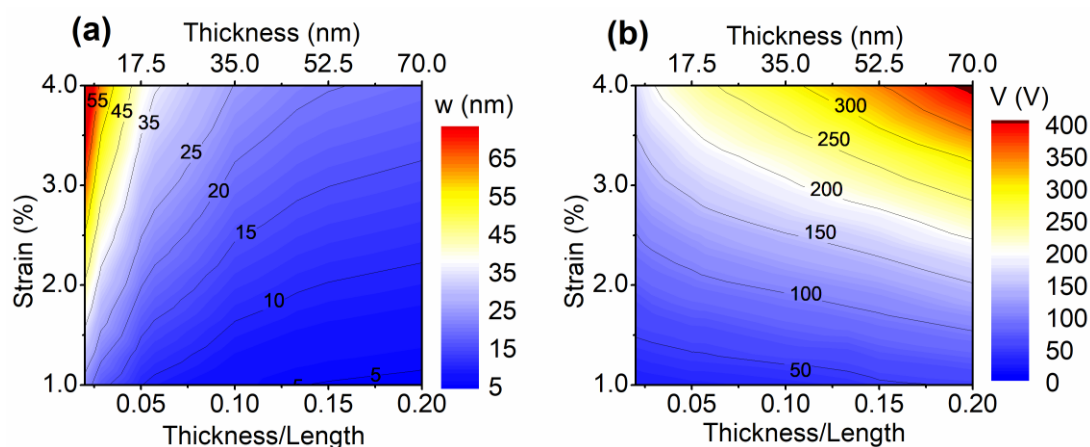
Figure 4.12. (a) The deflection at various axial strains and t/L ratios when geometric non-linearities are neglected in the simulations. The distance between the Ge nanobeam and Si substrate is equal to the 3 times of the deflection shown in (a). (b) The applied voltage at various axial strains and t/L ratios when geometric non-linearities are neglected in the simulations. The length of the nanobeam is 350 nm in (a) and (b).

4.3.3 Non-uniform Force Distribution

The third non-ideality is the non-uniform distribution of the electrostatic force. Although the SDT assumes uniform force distribution, the electrostatic force is partially focused at the center at high deflections. The spring constant of the nanobeam

is different for uniform load and the focused load at the center. To investigate the effect, the nanobeam under the electrostatic force is compared by FEM simulations with two cases: A nanobeam under the load uniformly distributed throughout the suspended region of the nanobeam, referred to as uniformly distributed load, and a nanobeam under the load completely focused to the bottom center of the nanobeam, referred to as point load (force is localization in x-axis < 4nm). .

In Fig. 4.13, the achieved deflections and strains for various voltages are presented for the uniformly distributed load, electrostatic load, and point load. Clearly, the deflections and strains are significantly higher than the electrostatic load and uniformly distributed load. The deflections and strains induced by electrostatic load are similar to the ones induced by the uniformly distributed load at small deflections. However, at higher deflections, the force localization enhance the deflections and strains achieved under electrostatic load, lying between the values achieved under uniformly distributed and point load.
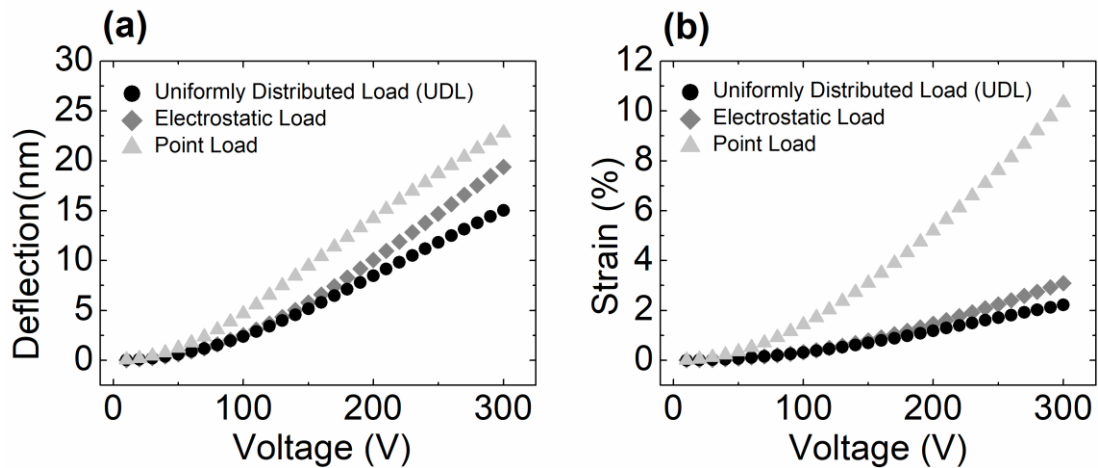
Figure 4.13. Variations of (a) the deflections and (b) strains with the applied voltage for a uniformly-distributed load along the Ge nanobeam, a point load at the symmetry axis and a load created by the electrical potential application. The length, thickness and, the gap distance values are 350 nm, 20 nm, and 100 nm respectively. The integration of uniform load and the electrostatic load over the length of the nanobeam and the magnitude of the point load are set to be equal.

It should be noted when point load is exerted on the bottom center of the nanobeam, Saint Venant's principle is no longer valid at that point and excessively

high amount of strain can be formed locally. The more practical force distributions will be less focused to a point and will result in more similar results although the trend remains the same. In this section, the completely focused case is used to compare the electrostatic loaf with two extremes.

4.4. The Strain at the Upper Portion of the Edges and Fillet Formation

As mentioned in Section 4.1.3, the tensile strain forms at three positions: lower portion of the center plane and upper portion of the edges of the nanobeam. However, the perfectly sharp corners at the edges where Ge nanobeam, SiO_2 layer, and the gap meet is not possible due to limitations during fabrication. The corners typically get rounded during wet etching as shown in Fig. 4.14, which remarkably effects the strain at the edges. The rounded regions at the edges are known as fillets.
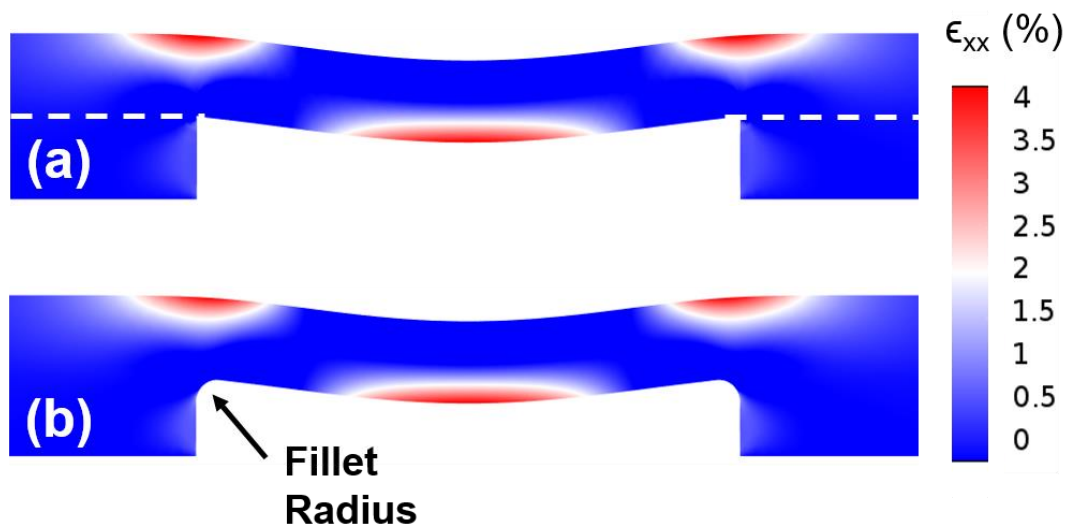
Figure 4.14. (a) Axial strain profiles on the Ge nanobeams without a fillet at the Ge nanobeam and SiO_2 corner and (b) with a fillet radius highlighted by the arrow, of 9 nm. Tensile axial strain at the bottom center is equal to 4% in (a) and (b). The length and thickness of the Ge nanobeam are 200 nm and 30 nm, respectively, in both (a) and (b). Dashed lines in (b) indicate the interface of Ge and SiO_2.

46

The change of the maximum strain at the upper portion of the edges with increasing fillet radius at 2% tensile strain at the bottom center of the beam is shown in Fig. 4.15. Although the strain at the edges reduces remarkably with increasing the fillet radius, it is generally higher than the strain at the bottom center of the nanobeam. Therefore, the strain values presented in this study are lower bound values.

Eq. 3.36 predicts the strain at the top of the edges as twice as higher than the bottom center of the nanobeam. However, the strain values at the upper region of the edges are much lower than the prediction even under perfectly sharp corners. The main reason is that the elasticity of the SiO_2 layer remarkably reduces the strain values at the top of the edges. As the thickness of the nanobeam increases, the force exerted on the SiO_2 layer increases. Therefore, the elasticity of the SiO_2 layer is more effective at the higher nanobeam thicknesses causing a less percentage of strain at the top of the edges.
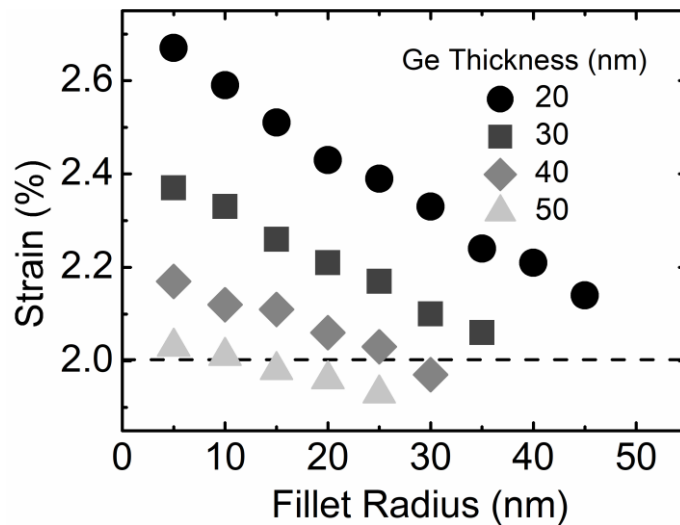
Figure 4.15. Variations of the axial strain at the two edges of the Ge nanobeam with fillet radius for Ge thicknesses of 20, 30, 40 and 50 nm, and a beam length of 350 nm. Axial strain at the bottom center of the nanobeam is independent of fillet radius and equal to 2%, indicated by the dashed line

CHAPTER 5

POSSIBLE FAILURE MECHANISMS

5.1. Dielectric Layer Utilization to Overcome Electric Breakdown

5.1.1 Electric Breakdown

Insulation of the terminals is a crucial part of any electrostatic or electromechanical system with two terminals. However, insulator materials utilized to separate two terminals cannot withstand the electric field intensity over a certain value referred to as electric breakdown field, E_{BD}. Although E_{BD} is almost constant for solid materials, known as dielectric strength, it changes with pressure and the gap distance of the terminals for the gases.

The breakdown of gases obeys a semi-empirical law called Paschen's law. Under an electric field higher than E_{BD}, the ionized atoms in the air make elastic collisions with neutral atoms and ionize them. The freshly ionized atoms also get energized under the electric field and ionize other neutral atoms creating an avalanche, also known as Townsend avalanche [76]. Moreover, the loss of electrons at the anode due to the avalanche is supplied by secondary electron emission so that breakdown is sustained. These physical phenomena lead to the formula of Paschen's Law

$$V_{BD} = \frac{Bpg}{\ln(Apg) - \ln(\ln 1 + 1/\gamma)} \qquad (5.1)$$

where V_{BD} is the breakdown voltage, p is the pressure, g is the gap distance, γ is Townsend's secondary ionization coefficient and A and B are gas constants. The change of breakdown voltage with the pressure-distance multiplication is shown in Fig. 5.1 for A=365 Torr^{-1}.cm^{-1}, B=25 V.Torr^{-1}.cm^{-1} and γ=0.01 [77].
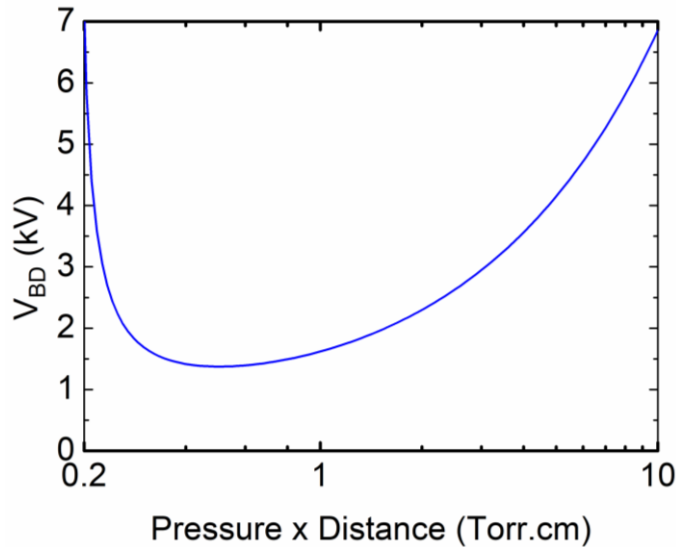
Figure 5.1. The change of breakdown voltage with pressure times gap distance multiplication according to Paschen's law.

The Paschen's law can be approximated to a line whose slope defines the E_{BD} for large initial gaps at constant pressure. For air, E_{BD} is reported as 30 kV/cm approximately [78]. However, the linearity comes to an end at moderate gap distances owing to the reduced mean free path of ions and as the distance further decreases, the ions cannot accelerate enough to ionize the neutral atoms with impact ionization and, thus, a rapid increase in breakdown voltage is expected. However, the experiments are not in agreement with Paschen's law for small gap distances [79], [80].

A well-accepted explanation of the deviation from Paschen's law at small gap distances is the participation of electrons emitted from the cathode as a result of enhanced field emission by ion movement through the cathode, ion-enhanced field emission, and Fowler-Nordheim field emission [81], [82]. Various articles supported the claim by demonstrating that field emission is capable of reducing the breakdown

voltage [83]–[85]. Moreover, as a result of field emission, the micro-plasma formation near the cathode is also introduced as a major cause of the breakdown [86], [87].

In the submicron regime, the electric breakdown changes linearly with the gap distance and 3.5 MV/cm of E_{BD} of air is reported [87]. Although the field emission is also major cause of the breakdown in a vacuum, much higher E_{BD} can be achieved compared to air as there are no neutral atoms to ionize or form a micro-plasma in vacuum (E_{BD} >50 MV/cm) [88].

In most electromechanical systems, electric breakdown is also a concern for solid dielectric materials which are utilized to mechanically support the terminals. Although the breakdown strength of solid dielectrics is typically much higher than that of air, for the structures operating in the vacuum, the breakdown of the solid dielectrics is more pronounced.

Among conventional insulators, SiO_2 has the highest E_{BD}. The silicon and oxygen atoms move in the opposite direction under the electric stretching the ionic bond between them under an electric field. The Si-O bond breaks when the stretching exceeds 20% of initial bond length which occurs at an electric field of 15 MV/cm [89], [90].

5.1.2 Overcoming Electrical Breakdown for Electrostatic Actuation

Operating under electric breakdown limit is also vital for the structure introduced in Chapter 4. The structure in Fig. 4.1 can be modeled with two capacitors: a capacitor filled with vacuum, $C_{vac,2C}$, with gap distance is g_{2C}, and a capacitor filled with SiO_2, $C_{ox,2C}$, and with gap distance equals to the gap distance of $C_{vac,2C}$. The average electric field can be obtained by dividing the required voltage to the gap distance, V/g_{2C}. Unfortunately, the required electric fields deduced from Fig. 4.4 mostly exceeds the breakdown strength of SiO_2.

One method to increase the gap distance while keeping the required voltage constant is to utilize dielectric layers in the gap as depicted in Fig. 5.2. The deposited

dielectric layer increases the number of capacitance to three and concentrates the electric field to upper capacitance.
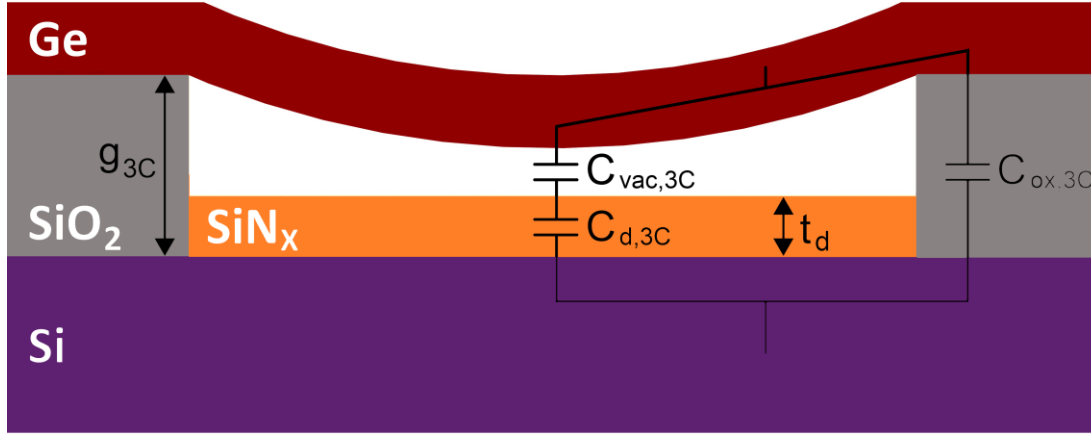
Figure 5.2 Cross-section schematics of the Ge nanobeam with SiN_x dielectric layer (with a relative permittivity ($\varepsilon_{r,SiNx}$) of 7.5) deposited on Si substrate. Capacitors associated with vacuum, dielectric layer and SiO2 are given. ϵ_d and ϵ_{SiO2} are the relative permittivity of the dielectric and SiO2, respectively

The capacitance filled with SiO_x is named as $C_{ox,3C}$ where the thickness of SiO_2 layer equals to g_{3C}, the capacitance filled with SiN_x is named as $C_{d,3C}$ where the thickness of SiN_x layer equals to t_d and the capacitance filled with vacuum is named as $C_{vac,3C}$. The electrical pressure with dielectric becomes

$$p = \frac{1}{2}\frac{dC''}{dz}V^2 = \frac{\epsilon_0 V^2}{2\left(g_{vac,3C} + \frac{t_d}{\epsilon_d} - w\right)^2} \tag{5.2}$$

The electrical pressure terms given without dielectric layer (Eq. 3.10) and with a dielectric layer (Eq. 5.2) become equal when

$$g_{vac,3C} + \frac{t_d}{\epsilon_d} - w = g_{eff} = g_0 = g_{vac,2C} \tag{5.3}$$

where $g_{3C,vac}+td/\epsilon_d$ is defined as the effective gap distance, g_{eff}. When the g_{eff} is kept constant, the same axial strain can be induced on the Ge nanobeam at the same voltage. However, the addition of dielectric layer cannot decrease the electric field on the vacuum since

$$E_{z,vac} = \frac{V}{g_{eff}} = \frac{\sigma_{vac}}{\epsilon_0} \tag{5.4}$$

where $E_{z,vac}$ is the electric field intensity on the vacuum and σ_{vac} is the surface charge density on the capacitor filled with the vacuum. When the g_{eff} is kept constant, both surface charge density and the applied voltage on the Ge nanobeam will be the same. However, since the $g_{ox,3C}$ is higher now, which is equal to

$$g_{vac,3C} + t_d = g_{eff} + t_d\left(1 - \frac{1}{\epsilon_d}\right) = g_{ox,3C} \tag{5.5}$$

The surface charge density at the edges can dramatically decrease with dielectric layer dimension resulting in reduced electric field intensity, which can be written as

$$E_{z,ox} = \frac{V}{g_{ox,3C}} = \frac{\sigma_{ox}}{\epsilon_0\epsilon_{ox}} \tag{5.6}$$

However, since there should be a vacuum region reserved for the deflection of the nanobeam, the limit of the dielectric thickness can be found as

$$t_{max} = \frac{2}{3}\epsilon_d g_{vac,2C} \tag{5.7}$$

5.1.3 Effect of the Dielectric Layer Thickness

The system with dielectric is simulated with FEM to support to claim that the maximum electric field can be reduced with this method. The electric field intensities for 350 nm length, 20 nm thickness, at the constant effective gap and various dielectric layer thicknesses are shown in Fig. 5.3a. As the dielectric layer thickness increases the maximum electric field intensity decreases. However, the electric field intensity deviates from the Eq. 5.6 since the equation neglects the fringing fields between $C_{vac,3D}$ and $C_{ox,3D}$. Another consequence of the fringing fields is that the required voltage is marginally modified due to the addition of the dielectric layer as it can be seen from Fig. 5.3b.

The electric field intensity distribution for 95 nm g_{eff} and 420 nm dielectric slab is depicted in Fig. 5.4. The concentration of the electric field to the vacuum can be seen clearly. Moreover, the field intensity on the SiN_x is approximately $1/\epsilon_d$ times of the field intensity in the vacuum. Thus, the dielectric breakdown of the SiN_x is not a concern. Furthermore, the addition of dielectric layer reduces the gap filled with vacuum and therefore increases the breakdown field of the vacuum [88].
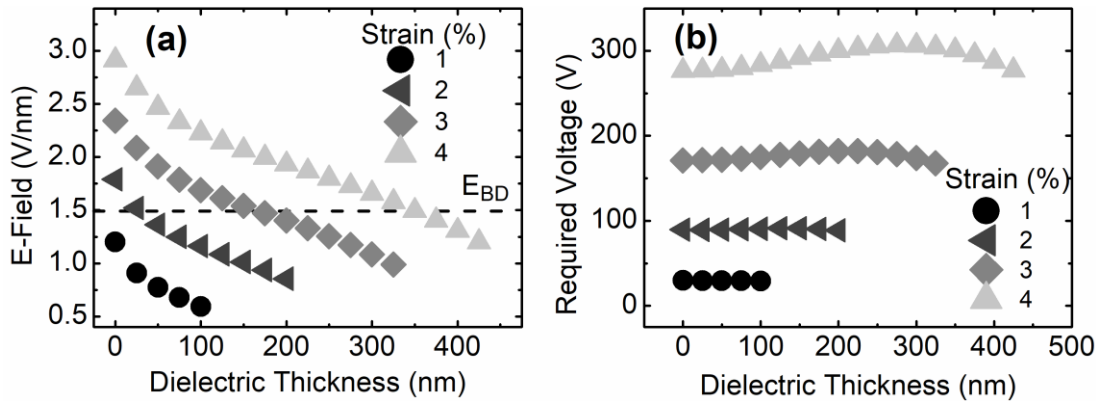
Figure 5.3 (a) maximum electric field to achieve 1, 2, 3 and 4% axial strain at constant g_{eff} (25 nm, 50 nm, 73 nm, 95 nm, respectively) for varying dielectric layer thicknesses and at L=350 nm, t=20 nm and the deflection is set g_{eff}/3 (b) The change of the required voltages with the dielectric thickness to achieve 1, 2, 3, and 4% tensile strains at the symmetry axis of the Ge nanobeam.
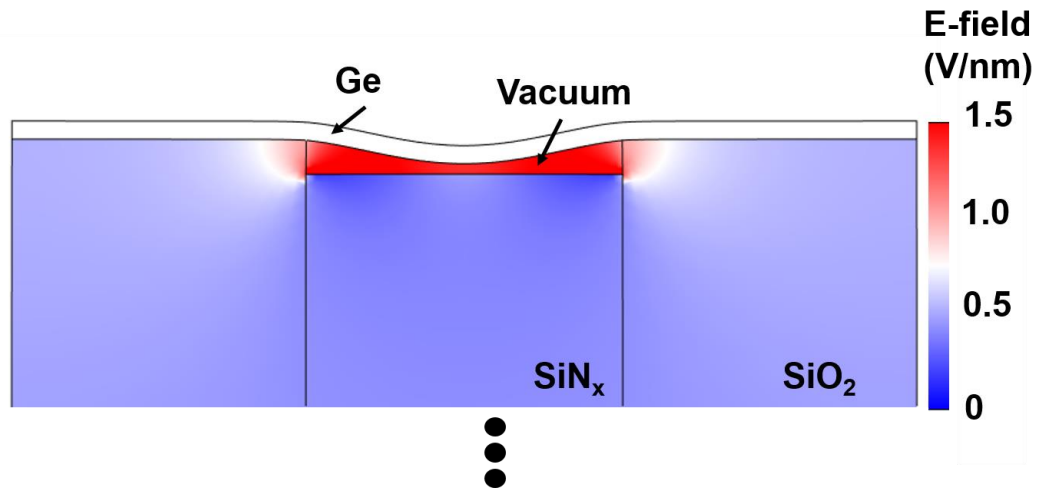
Figure 5.4 The 2D color graph of electric field intensity distribution throughout the structure for 350 nm of length, 20 nm of thickness, 95 nm of effective gap distance and 420 nm dielectric thickness.

5.2. Mechanical Fracture

The mechanical stability of the beams is also essential for any reliable system and the material should be able to keep itself intact to maintain the stability. However, the nanobeam structures similar to the one introduced in Chapter 4 can fracture under large deflections. The maximum stress before fracture occurs is called as tensile strength. Yet, for structures like beams which operate by deflected transverse rupture strength is used instead since the stress is not uniform throughout the structure.

Ge is a brittle material under moderate temperatures and hardly exhibits any ductility. Moreover, the ideal tensile strength of Ge is reported to be quite high, around 14-20 GPa [12], [91]. Although bulk Ge typically fractures at much lower stresses than its ideal tensile strength, nanobeam structures can be fabricated with much lower defect concentration and hence, can stand much higher stresses than bulk Ge [92], [93]. For nanowires, 17% flexural strain, corresponding transverse rupture strength of 18 GPa is demonstrated [93].

The first principal stress distribution of Ge nanobeams is shown in Fig. 5.5. The stress is maximized at the two upper edges and the bottom center as expected. It can be seen that the maximum stress values are much smaller than the transverse

rupture strength of Ge. Moreover, the tensile stresses at the edges are less than twice of the stress at the bottom center of the nanobeam thanks to the elasticity of the SiO₂ layer.
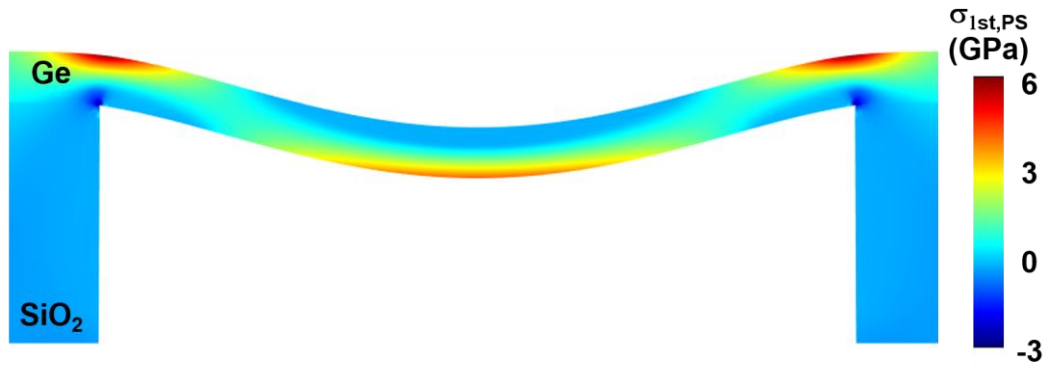
Figure 5.5. 1st principal stress profile of Ge nanobeam and SiO₂ layer for 350 nm length 20 nm thickness and at 4% tensile strain at the bottom center of the nanobeam.

CHAPTER 6

REDUCING THE REQUIRED VOLTAGE BY MODIFYING THE NANOBEAM STRUCTURES

The required voltages to induce relatively high strains (>2%) on Ge nanobeams by electrostatic actuation is typically over 100 V for lengths higher than 200 nm. However, such high voltage values might not be practical for the design of electro-optic IC. Therefore, two different ideas are investigated in this chapter.

6.1. Electrostatic Actuation of the Initially Strained Structure

One method to reduce the required voltage is to combine the electrostatic actuation with the other strain induction methods similar to the ones introduced in Section 2.1. If some portion of the required strain to achieve a certain level of light enhancement can be provided via other methods, the required voltage to provide the additional strain could be much lower. From this standpoint, a tensile strain induction method utilizing a stressor layer is introduced in this section and the reduction of the required voltage is showed.

6.1.1 Structure

A structure to induce an initial strain on Ge nanobeams is shown in Fig. 6.1. A SiN_x layer with 1.5 GPa tensile stress – a value which has been reached in the literature before [94], [95]- is assumed to be deposited on Ge nanobeams and patterned so that it covers the Ge beam resting on the SiO_2 layer and some portion of the suspended region at the edges. The tensile stress on the SiN_x layer reorganizes itself such that tensile strain is induced on suspended Ge nanobeam not covered by SiN_x to balance the stress on SiN_x layer.

57

The SiN$_x$ layer is typically much thicker than Ge nanobeam and prevents the deflection at the region. Therefore, the length of the Ge nanobeam is defined as the region of the Ge which is not covered with the SiN$_x$ layer.

As the stress on the SiN$_x$ layer reorganizes itself, the nanobeam initially gets bent away from the Si substrate which consequently increases the gap distance between the center of the beam and Si substrate as it can be seen from Fig 6.2a. Therefore, the gap is considered as the summation of the thickness of SiO$_2$ and the initial deflection occurring at the center of the nanobeam due to the reorganized stress of SiN$_x$.
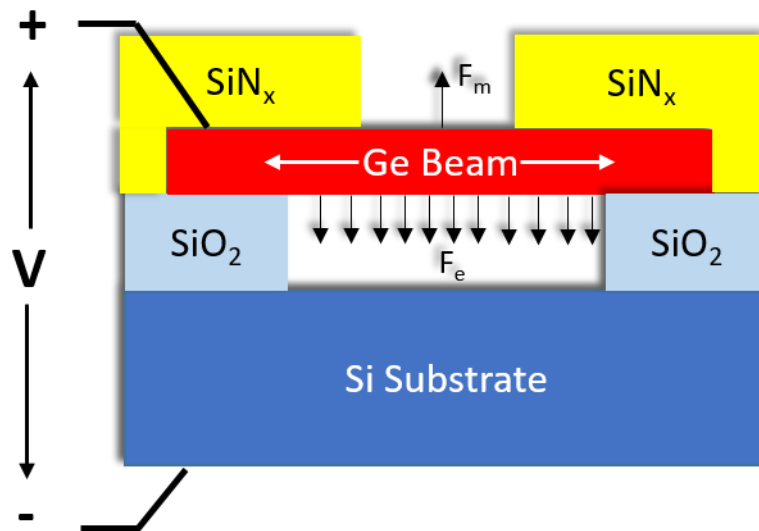
Figure 6.1. Cross-sectional schematic of the Ge nanobeam suspended from both sides by SiO$_2$, and initially strained by a SiN$_x$ layer, and in the presence of an electrostatic force. White arrows indicate tension introduced by SiN$_x$. Plus and minus signs represent positive and negative charges accumulated as a result of applied voltage at the nanobeam and substrate, respectively.

The stress induced on Ge nanobeams by tensilely stressed SiN$_x$ layers is uniformly distributed throughout the nanobeam except for 2 edges where the nanobeam meets the SiN$_x$ layers as it can be seen from Fig. 6.2. After electrostatic actuation, however, the strain distribution loses its uniformity and the strain localization at the bottom center of the nanobeam is observed.
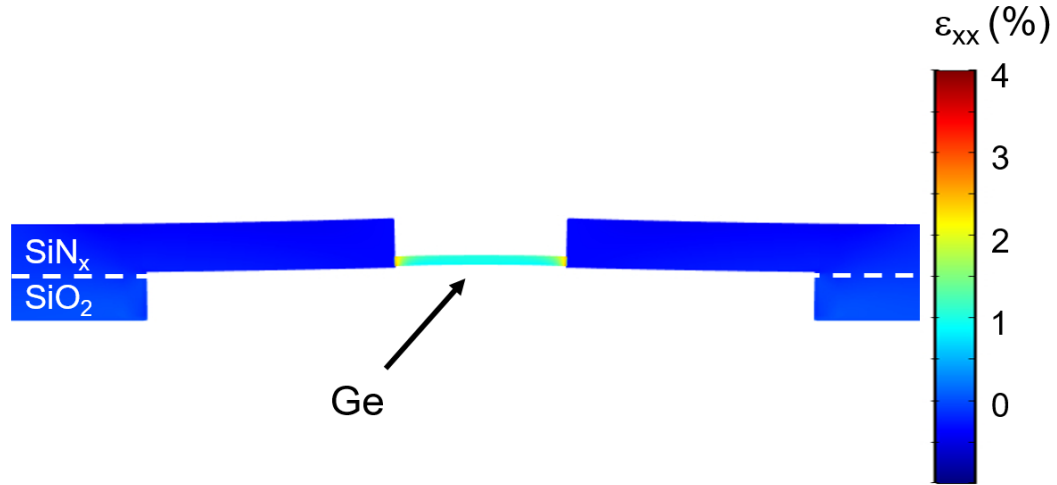
Figure 6.2. Strain profile of Ge nanobeams with stressed SiN_x layer before electrostatic actuation for 350 nm of length, 20 nm thickness and uniform 1% initial tensile strain throughout the beam.

6.1.2 Effect of Dimensions to Induced Initial Strain

The percentage of the induced strain mostly depends on 4 dimensions: thickness of the nanobeam, denoted with t, thickness of the SiN_x layer, denoted with t_N, the separation between the SiO_2 layers, L', and the separation between the SiN_x layers, which corresponds to length of the beam, L, as depicted in Fig. 6.3. The effects of changing the dimensions are analyzed with 2D FEM simulations in this section. How strain changes with t_N and L' for various t and L values and is shown in Figs. 6.4a and 6.4b, respectively. The strain increases sublinearly with the t_N and with decreasing t. Moreover, the strain also increases with decreasing L. Among all, the most dominant effect, however, is the changing L'. As it can be seen in Fig. 6.4b, the induced strain increases linearly with L' and strain values higher than 5% can be achieved for t=20 nm, t_N=550 nm, L=175 nm, and L'=2800 nm.
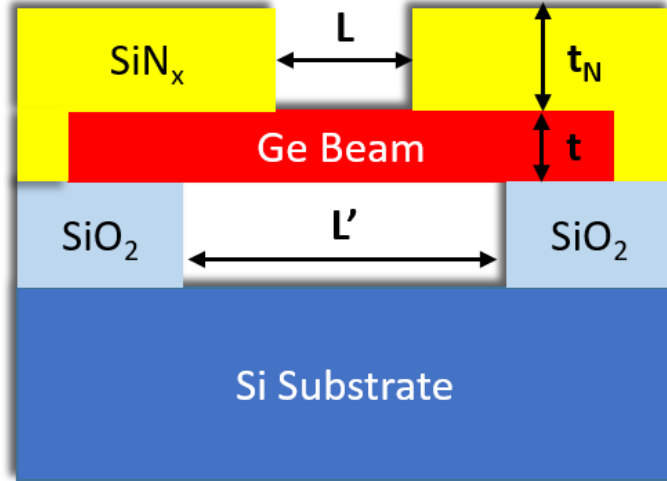
Figure 6.3. A cross-sectional schematic of the initially strained Ge nanobeam structure with indicated denotations.

Together with the 4 major dimension effect, the widths of the SiN_x layer and Ge nanobeam, the total length of SiN_x of Ge also marginally affects the strain up to some point (not shown here), they are all taken is sufficiently large so that their effect can be neglected.
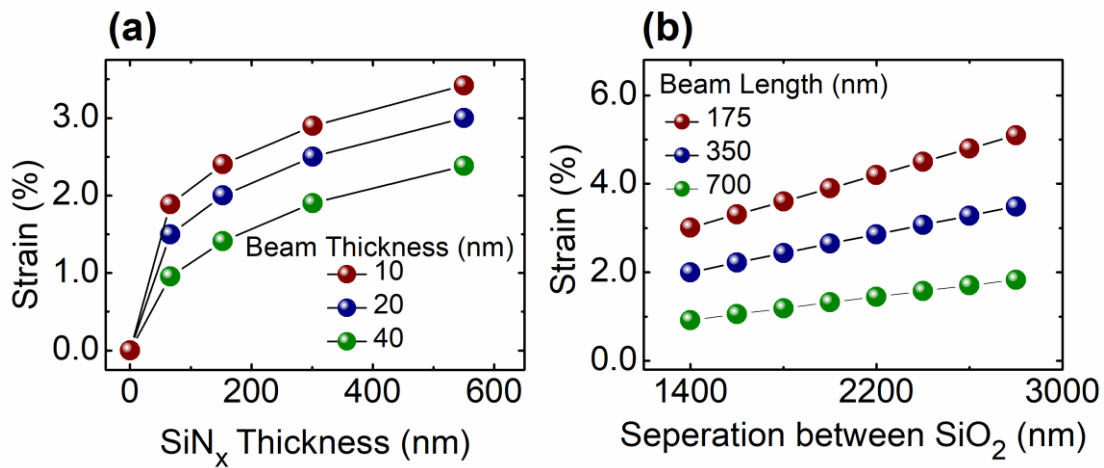
Figure 6.4 (a) The change of strain with SiN_x thickness for the nanobeam length of 350 nm, the separation of SiO_2 layers of 1400 nm and the nanobeam thicknesses of 10, 20 40 nm. (b) The change of strain with the separation of SiO_2 layers for the nanobeam thickness of 20 nm SiN_x thickness of 180 nm and for the nanobeam lengths of 175, 350 and 700 nm.

6.1.3 Electrostatic Actuation of Initially Strained Ge Nanobeams

Although the structure seems to be capable of achieving sufficient tensile strains to modify Ge to direct bandgap, there might be fabrication-wise limitations in reality. Especially, obtaining L' higher than L probably requires the underetching of SiO_2, and thus, it might be challenging to achieve high L'/L ratios. Therefore, the fabrication-wise limitations might prevent to achieving relatively high strain values. The remaining required strain can be provided via electrostatic actuation, which would also introduce post-fabrication tunability.

To determine the required voltages to achieve 4% tensile strain, 3D FEM simulations are run and the results of the strain at the bottom center of the beam are presented in Fig. 6.5. It should be noted that the nitride thicknesses to reach desired strains are in agreement with the 2D simulations shown in Fig. 6.4.

It should be also noted that the required voltages are not presented at the constant gap but they are modified so that the thickness of the SiO_2 layer is set to three times of the required deflection to achieve each strain value. Moreover, the gap distance is not the same as the thickness of the SiO_2 as explained in Section 6.1.1. The deflection used to determine the gap distance is defined as the displacement of the nanobeam after electrostatic actuation.

The required voltage to reach 4% tensile strain decreases expectedly as the initial strain increases. At 3% tensile strain the required voltage to reach 4% tensile strain drops to 66V from 276 V at no initial strain. However, the voltage required to induce additional 1% tensile strain from 3% to 4% is higher than the voltage required to reach 1% tensile strain from unstrained nanobeam. The major reason for the discrepancy is the stress stiffening of the nanobeam. As 3% tensile strain is induced, the stiffness of the beam increases and it gets harder to deflect.
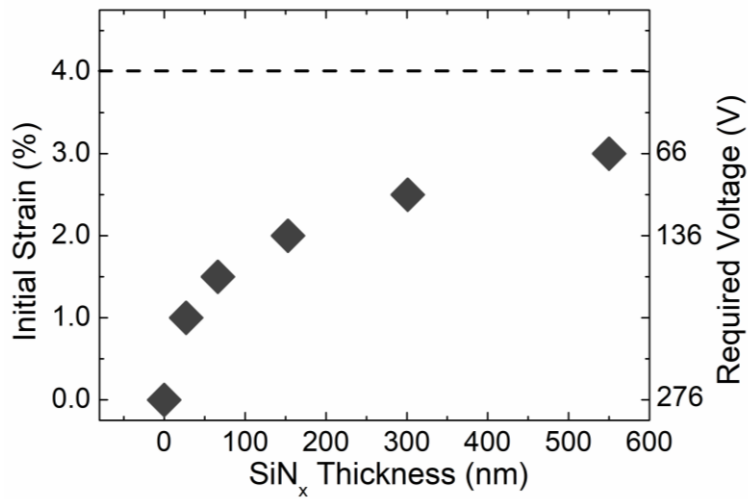
Figure 6.5. The change of initial strain with SiN_x thickness for 100 nm of SiO_2 thickness with the voltages required to achieve 4% tensile strain for 350 nm of L, 20 nm of t, 200 nm of b, 1400 nm of L', deflection equals to g/3 and 0, 2 and 3% initial strains.

6.2. Structures to Induce Biaxial Strain

Since the required biaxial strain to modify Ge to direct bandgap is even less than 2%, the voltage required to obtain the same light emission enhancement can be reduced with a structure which would induce biaxial strain instead of uniaxial strain upon deflection. Thus, in this section, two structures to induce strain are investigated, namely cross-shaped nanobeams and rectangular membranes. The biaxial strain is calculated as the arithmetic average of the uniaxial strains as used in the article of Gassenq et al. [96]. The structures are compared with each other and the uniaxial strain of the nanobeam. The elasticity of SiO_2 is ignored throughout this section for the sake of simplicity.

6.2.1 Cross-Shaped Nanobeam

The structure is defined as the intersections of two nanobeams with 350 nm length, 88 nm of width (L/4) and 20 nm of thickness perpendicular to each other as shown in Fig. 6.6. The nanobeams are fixed from all four edges. Upon the applied voltage, almost uniformly distributed strain is induced at the bottom surface of the intersection region of the Ge nanobeams.
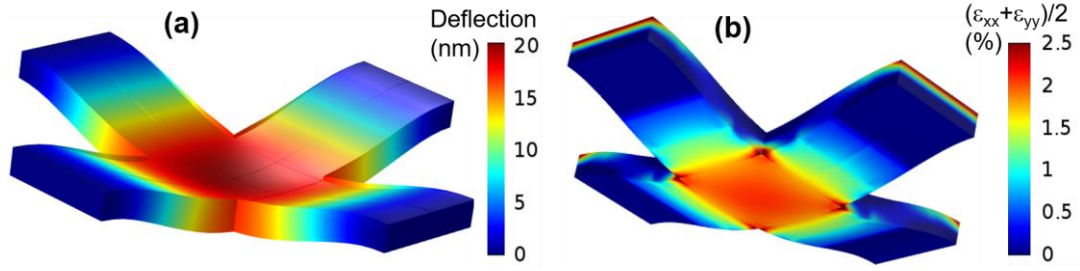
Figure 6.6. (a) The deflection profile of the upper surface and (b) the strain profile of the lower surface of the electrostatically actuated cross-shaped structure at 2% biaxial strain at the bottom center of the structure consisting two nanobeams with 350 nm length 88 nm of width and 20 nm of thickness.

The required voltages to reach the predetermined biaxial strains for the structure shown in Fig. 6.6 are presented in Fig 6.7b for two conditions: the deflection equals to one-third of the gap distance and the structure operates at the verge of pull-in. The associated gap distances are also shown in Fig. 6.7a.

Since the structure is fixed from all four edges instead of two, a higher amount of strain can be induced at smaller deflections; and therefore, the effect of large deflection theory is milder. Although the exact predictions are different than the nanobeams introduced in Chapter 4, the trends seem to be in agreement with the small deflection theory. At deflection equals to the one-third of the gap condition, the required voltages fit approximately to the biaxial strain to the power 1.5, $\epsilon_{bi}^{1.5}$.

At the verge of pull-in, approximately 18 nm of deflection is required which is very close to the thickness of the nanobeams. Therefore, stress stiffening is also active at high strains which extends the pull-in distance. The increase in the pull-in distance reduces the dependence of the required voltage on the biaxial strain to $\epsilon_{bi}^{1.25}$. The required voltage to achieve 2% tensile strain can go down from 146V to 82 V by operating closer to pull-in, which occurs approximately at the half gap distance.

In Fig. 6.6b, it can be seen that strain locally increases at four corners of the intersection region. However, the strains at the sharp corners are not meaningful as the corners get rounded during the etching. Similar to the discussion in Section 4.4, the fillet formation at the corners affects the percentage of tensile strain at these points. Therefore, the main focus is again at the bottom center of the cross-shaped structure.
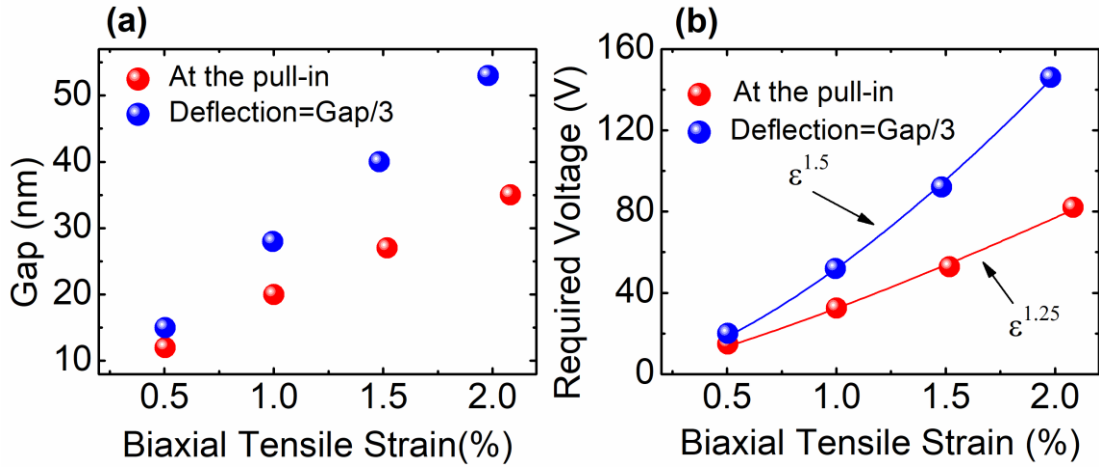
Figure 6.7. (a) The gap distances that should be set and (b) at the associated gap distances, the voltages required to achieve predetermined biaxial strain values for the cross-shaped structure operating at the verge of pull-in and under the condition of $w=g_0/3$. Allometric fits of the required voltages are shown with solid lines.

6.2.2 Square Membrane

Another structure to induce biaxial tensile strain upon deflection is a Ge membrane. The membrane is chosen as a square with 350 nm side length, with all the edges assumed to be perfectly clamped. The deflection and the strain profile of the top and bottom surface of the membrane are shown in Fig. 6.8a and 6.8b, respectively.
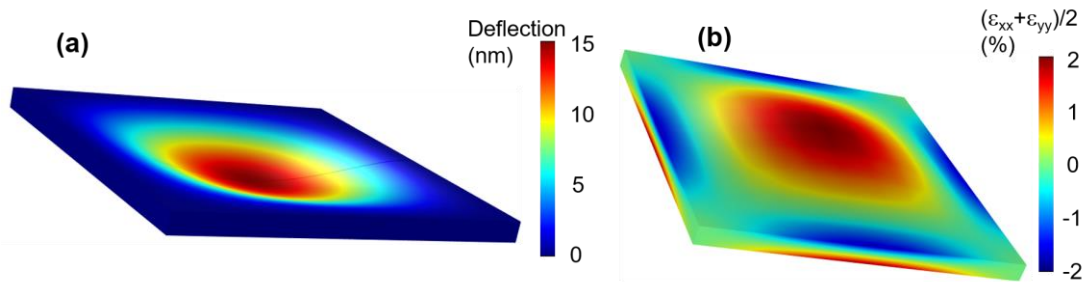
Figure 6.8. (a) The deflection profile of the upper surface and (b) the strain profile of the lower surface of the electrostatically actuated square membrane at 2% biaxial strain at the bottom center of the structure for the side lengths of 350 nm and the Ge thickness of 20 nm.
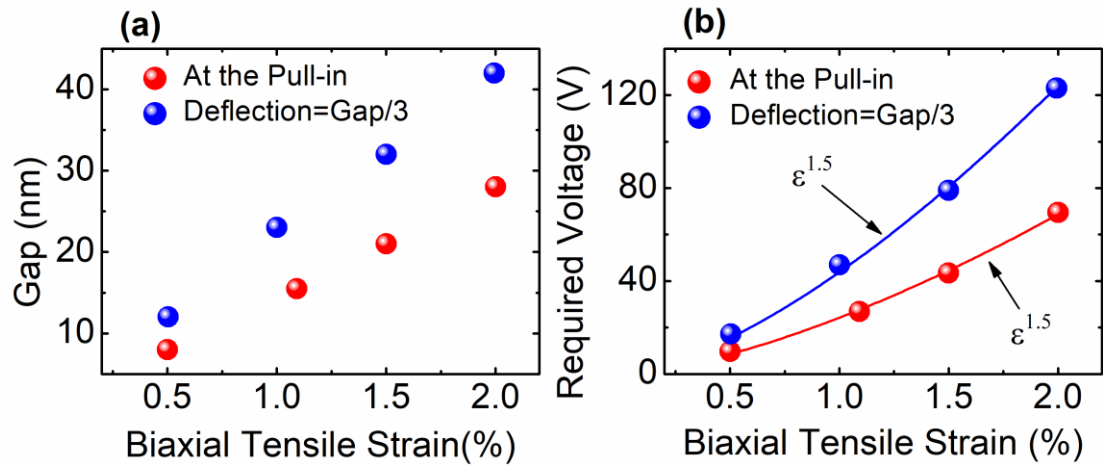
Figure 6.9. (a) The gap distances that should be set and (b) at the associated gap distances, the voltages required to achieve predetermined biaxial strain values for the square membrane operating at the verge of pull-in and under the condition of deflection equals to one-third of gap distance. Allometric fits of the required voltages are shown with solid lines.

The membranes are much stiffer than the nanobeam structures yet the higher amount of strain is formed at the same deflection. The required gaps and voltages to reach predetermined biaxial tensile strain at the verge of the pull-in and under the condition that deflection equals to one-third of the gap distance are presented in Figs. 6.9a and 6.9b, respectively.

The required deflections are even less than the cross-shaped structure and hardly comparable with the thickness, eliminating the stress stiffening effect. Therefore, the pull-in distances remain constant as half of the gap distance as the desired strain increases. As a result, both conditions fit to stain to the power 1.5, $\epsilon_{bi}^{1.5}$. Similar to the cross-shaped beam, by operating closer to the pull-in the required voltage to reach 2% tensile strain drops to 69.5V from 123 V.

6.2.3 Overall Comparison

The required voltages for cross-shaped structure, square membrane, and nanobeam under the condition that deflection equals to one-third of the gap distance and at the verge of pull-in are presented in Figs. 6.10a and 6.10b, respectively. For a

fair comparison, the elasticity of SiO$_2$ is neglected in all of the cases. The width of the beam is set to 88 nm (L/4).

Comparing with the uniaxial strain of the Ge nanobeam, the required voltages to achieve the same amount of biaxial strain is significantly higher. However, it requires higher uniaxial strain to achieve the same energy difference between conduction band minima of Γ and L valleys. Thus, when the required voltages to achieve 2% biaxial tensile strain for cross-shaped structure and square membrane are compared with the required voltage to achieve 4% uniaxial tensile strain for Ge nanobeam, it can be seen that significant reduction in the required voltage can be satisfied.

It should be noted that the pull-in distance extension due to stress stiffening in nanobeam structure is more massive than the other structures causing the huge gap at 2% tensile strain. However, at higher Ge thicknesses, the nanobeam structure cannot reach the pull-in distance of other structures; and therefore, the structures to form biaxial strains will be even more advantageous.
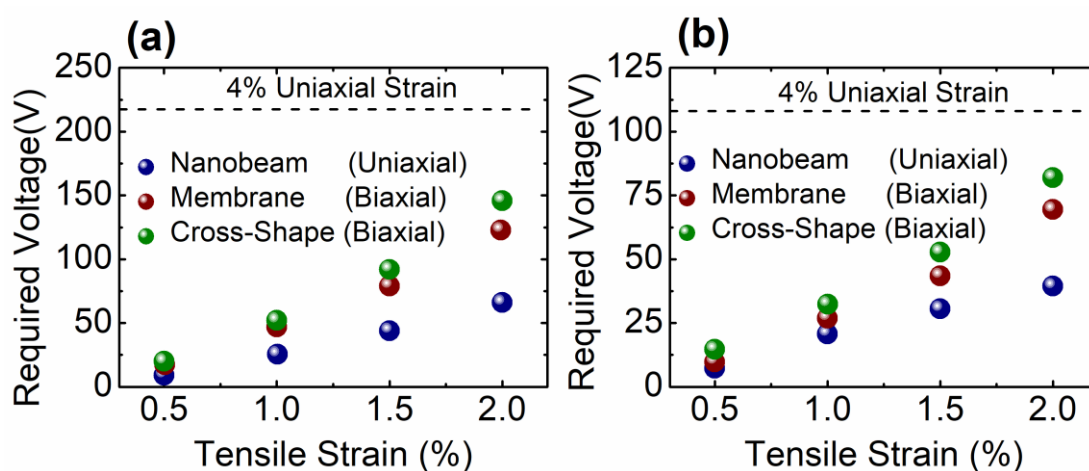
Figure 6.10. The required voltages to achieve predetermined strain values for the condition of (a) g=3w and (b) at the verge of pull-in. The dashed lines show the required voltage to achieve 4% uniaxial strain with the Ge nanobeam under each condition.

66

CHAPTER 7

ELECTRICAL ANALYSIS OF THE NANOBEAM STRUCTURE

The strain profile on the deflected beams create are non-uniform as shown in Fig. 4.4. As the maximum energy shrinkage between the bottoms of the conduction band at Γ and L valleys are obtained as the highest strain points. Therefore, only a small portion of the beam participates in light emission. However, the carriers at the other regions will be localized to highest strain regions as a result of formed pseudo-heterojunction where the recombination is maximum. In this chapter, the radiative recombination velocities are analyzed with electrical FEM simulations on the SILVACO ATLAS platform to quantify the effect of carrier localization and to compare the emitted light intensity of deflected nanobeams with the uniform strained ones.

The nanobeam is selected to have 200 nm of length, 30 nm of thickness and 9 nm of fillet radius at the edges so that the maximum strain at the edges and at the center plane of the nanobeam is the same. The maximum strain achieved in the bent structure is set to be equal to the strain of the uniformly strained structure. The bandgap shrinkage with the tensile strain is modeled according to previous experimental studies [36]. The bandgap change with the compressive strain is ignored in this section as the effect of the local bandgap increase is expected to be low and as there are no experimentally proven bandgap change for the compressive strain induction. The direct bandgap profile of the bent beam is depicted in Fig. 7.1. In the analysis, the radiative recombination from the bottom of the conduction band at L valley is neglected. Therefore, the radiative recombination rate of the unstrained Ge is slightly underestimated although the radiative recombination rate of the strained Ge is not expected to change much. The optical generations are taken as solely in the Γ valley throughout the rest of the simulations. Since the total density of states of L valley is approximately 56 times of that of the Γ valley, the total corresponding optical

generation is nearly two orders of magnitude higher than the optical generations at the Γ valley. Surface recombination is ignored in the discussion since it can change with the passivation techniques. The Auger coefficients for holes and electrons are taken as 3×10^{-32} cm^6/s and 7×10^{-32} cm^6/s, respectively [25].

The profiles of the ratio of radiative recombination rate enhancement via a deflection on half of the nanobeam for various strains are shown in Fig. 7.2. As the strain difference increases, the localization of the carriers to the highest strain regions becomes more pronounced and the radiative recombination rate at these regions can be enhanced more than 10000 times. The radiative recombination rate at the regions with small strain decreases remarkably due to lack of carriers triggering recombination. Although the regions where light emission enhancement is obtained are much smaller than the lightly strained regions, the cumulative radiative recombination is expected to rise remarkably.
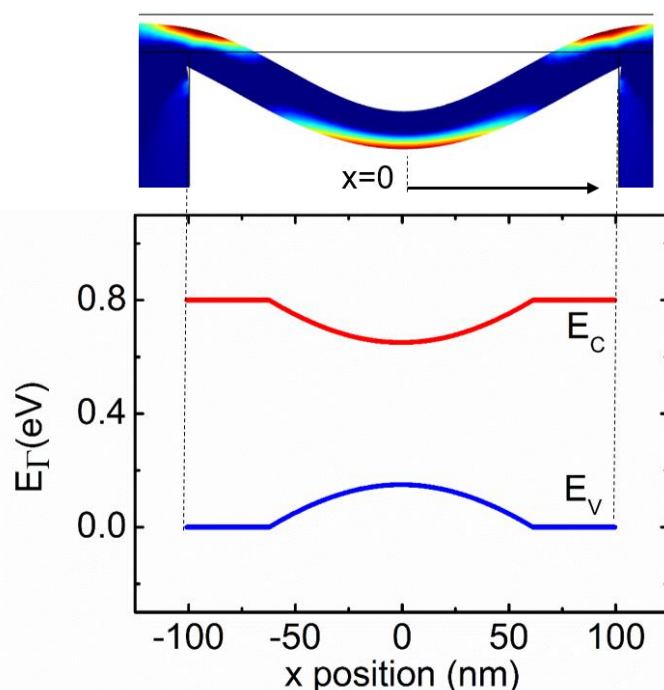
Figure 7.1. The calculated bandgap profile of the bottom surface of the Ge nanobeam with 200 nm length and 30 nm thickness. The uniaxial tensile strain at the bottom center is 4%.

68
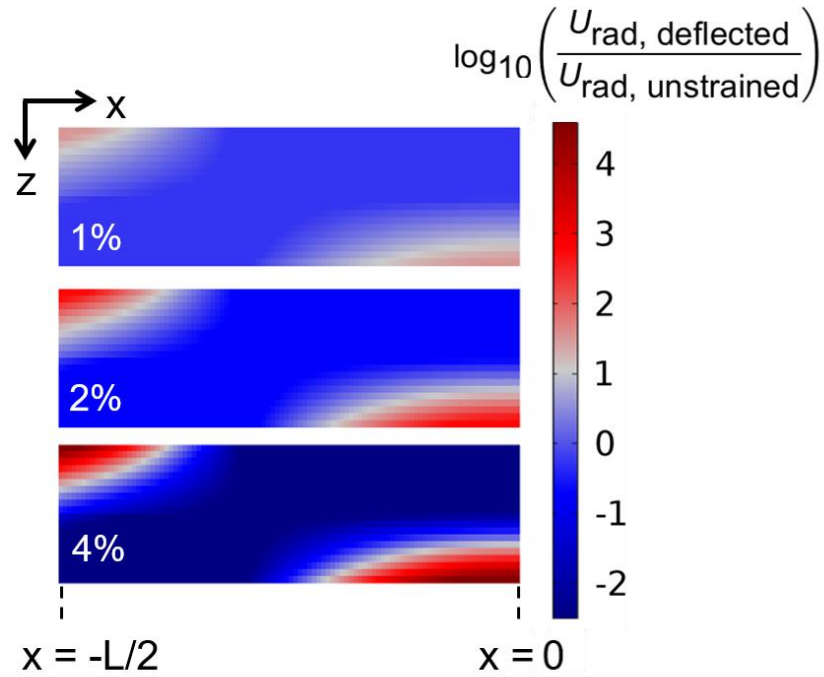
Figure 7.2. The profile of the ratio of the radiative recombination rate of the deflected nanobeam to that of the unstrained nanobeam for 200 nm length and 30 nm thickness and the uniaxial tensile strain at the bottom center is 1, 2, and 4% at 10^{27} cm^{-3}.s^{-1} optical generation in the Γ valley.

The percentages of the recombination mechanisms and the change of the cumulative radiative recombination rate with the tensile strain are shown at various optical generations in Fig. 7.3a and 7.3b. At the small optical generations, Shockley-Read-Hall (SRH) recombination mechanism dominates due to lack of carriers. However, as the number of carriers increases as a result of increasing optical generation, the radiative recombination increase remarkably. However, Auger recombination starts to dominate at very high optical generations decreasing the radiative recombination. Thus, the percentage of the radiative recombination has a local maximum around 10^{28} cm^{-3}/s. The portion of the radiative recombination does not exceed 5% of the total recombination even under 4% tensile strain as it can be seen in Fig. 7.3b. Although this result signals that the nanobeams will typically require high carrier injections, they can still offer better light emission behavior potentially than the uniformly strained structures.
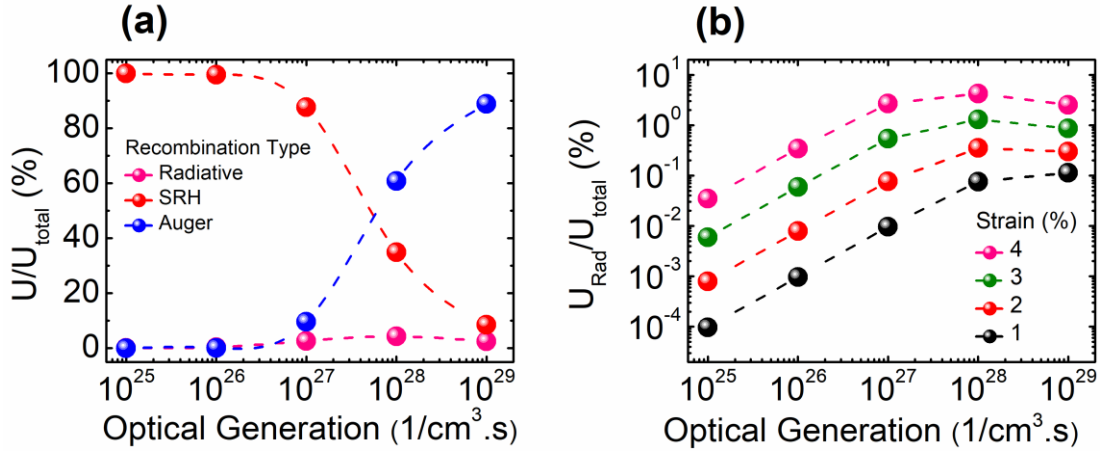
Figure 7.3. (a) The change of the ratio of the various cumulative recombination mechanisms with optical generation and (b) the change of the ratio of the cumulative radiative recombination with optical generation for various tensile strains. The dashed lines are guide to the eye.

The enhancements of light emission to the unstrained nanobeams by electrostatic actuation for various optical generations are shown in Fig. 7.4a. The cumulative radiative recombination rate of the nanobeam structure increase with approximately ten to the power of strain at small optical generations. However, as the optical generation increases, the enhancement start to decrease as a result of increasing Auger recombination. Therefore, the light emission enhancement is more pronounced at the small optical generations.

The ratios of the cumulative radiative recombination rate of the electrostatically actuated nanobeams to the uniformly strained structures are shown in Fig. 7.4b. At 1% tensile strain, the effect of carrier localization is not very significant so that the effect of the emission volume dominates. Therefore, uniform strain profile results in higher radiative recombination rate cumulatively. However, as the strain increase, the effect of carrier localization becomes much more effective and the high carrier densities at the highest strain points of the bent nanobeam boost the radiative recombination rate at small optical generations. However, at the high optical generations, the carrier density at the highest strain locations become so excessively high that most of the excess carriers lost with Auger recombination dramatically reducing the radiative recombination rate. Therefore, uniformly strained structures are more advantageous at high optical generations.

70
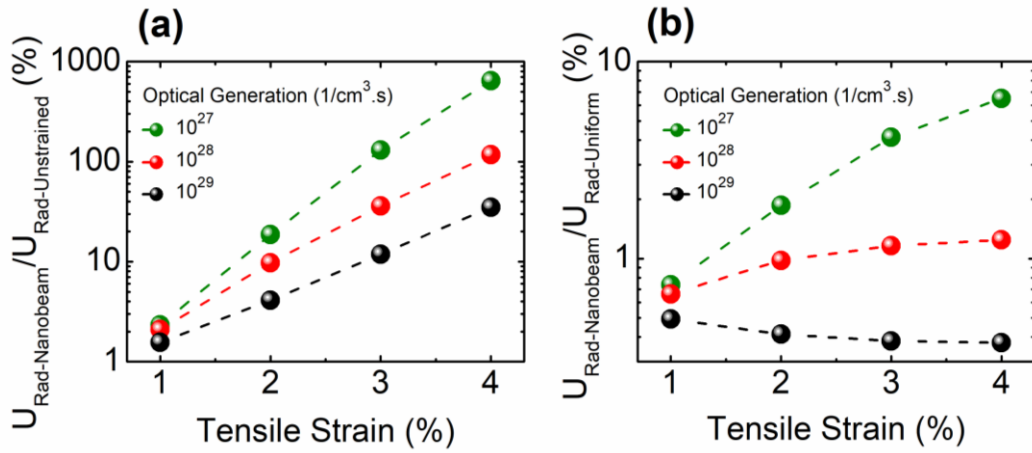
Figure 7.4. (a) The change of the ratio of the various cumulative recombination mechanisms with optical generation and (b) the change of the ratio of the cumulative radiative recombination with optical generation for various tensile strains.

At the optical generations lower than 10^{27} cm^{-3}.s^{-1} and 4% tensile strain, electrostatically actuated nanobeams offer 800 times higher cumulative radiative recombination comparing to unstrained nanobeams and 8 times higher comparing to uniformly strained structure thanks to the carrier localization. Therefore, electrostatically actuated nanobeams show great potential in the low-threshold optical devices.

CHAPTER 8

CONCLUSIONS AND FUTURE WORKS

In this thesis, a Ge nanobeam actuator is introduced allowing post-fabrication tunability and IC compatibility. The required deflections and voltages are provided by FEM simulation with the effects of changing dimensions. The physical mechanisms of the structure are compared with the theoretical approximations and the deviations are investigated with the simulations as well. The mechanical and electrical failure mechanisms of the structure are also investigated. The electric breakdown possibility which could be a serious problem at high tensile strains can be reduced by utilizing a dielectric layer partially covering the gap. Furthermore, the methods are proposed to reduce the required voltage: Reducing the required uniaxial strain induced by electrostatic actuation by initially straining the Ge nanobeam with a structure utilizing stressor layer or utilizing a structure that would introduce biaxial strain instead of uniaxial strain as the required biaxial strain is lower for Ge to achieve the same amount of light emission enhancement. An exemplary structure to reduce to induce initial strain on Ge nanobeam and two fundamental structures to induce biaxial strain upon electrostatic actuation, a cross-shaped structure and a membrane, are investigated. Finally, electrical analysis of the formed non-uniform bandgap profile is investigated and the light emission performance of the bent nanobeams can even exceed the light emission performance of uniformly strained nanobeams under medium optical generations and at high tensile strains.

Although the required strain to achieve direct bandgap is around 4.7%, no abrupt light emission enhancement is observed at that percentage. A sharp drop in the threshold power is estimated at around 3.1% uniaxial tensile strain due to valance band splitting effects [36], [97]. The required uniaxial strain values can be further reduced by Sn incorporation and n-type doping. Similarly, a structure to induce biaxial strain can be also utilized such as cross-shaped fixed-edge structure and the required voltages can reduce to even smaller values. Moreover, the initial strain induction can be also

73

applied to structures formed to induce biaxial strain upon electrostatic actuation to further reduce the required voltage.

The post-fabrication tunability of the introduced method is also quite significant as the materials operating under stress typically deforms with the creep process. The deformation alters the strain on the structures changing the wavelength of emission. Therefore, the occurrence of the creep can significantly shorten the life-span of the structure. However, by sensing the light emission profile, a feedback loop can be formed to maintain the same strain level on Ge nanobeam.

The structures typically have an inevitable strain gradient through the structure although it can be minimized as a result of stretching. Even though the small portion of the nanobeam is actually under the strain that can provide optical gain, the carrier localization to highest strain points can greatly improve the optical gain at these locations as long as Auger recombination rate is low and the efficiency of the graded strain structure can be comparable with the uniformly strained structure.

The simulations made in this thesis creates a detailed picture of the strain induction on Ge nanobeams by electrostatic actuation. Most effects are discussed with the ways of overcoming failures and reducing the required voltage. The simulations can be extended, however, by utilizing 3D simulations and presenting a larger map including the width of the beam. The effect of contacts can be also included to model to improve the accuracy of the simulations. Furthermore, the maps of the required voltages for the cross-shaped structure and the membrane with the simulations including the elasticity of SiO_2 can provide a better low-required-voltage solution which can be customized.

Another important breakthrough of this study will be the actual demonstration of the light emission enhancement with this method. An exemplary fabrication method is introduced here. Starting from a germanium-on-insulator (GOI) substrate as depicted in Fig. 8.1a, which is commercially available, a photolithography is made to define the nanobeam shape in this model. Then, the uncovered Ge regions on the GOI substrate is etched with reactive-ion-etching so that the shape in Fig. 8.1b is obtained. After that, another photolithography step is made to define the contact areas together with the deposited Ag layer and the lift-off process (Fig. 8.1c). Later, another Ag deposition with thermal evaporation is made to obtain back contact (Fig 8.1d). It is

noted that edge isolation is crucial to prevent the short circuit formation and both semiconductors are assumed to be heavily n-doped. Lastly, undetching of the SiO_2 is subsequent to another photolithography step to obtain suspended Ge nanobeam (Fig. 8.1e). Two top contacts are connected to positive bias and the bottom contact is connected to negative bias or vice-versa. The fabricated structure also should operate in the vacuum; therefore, it should be sealed in the vacuum.
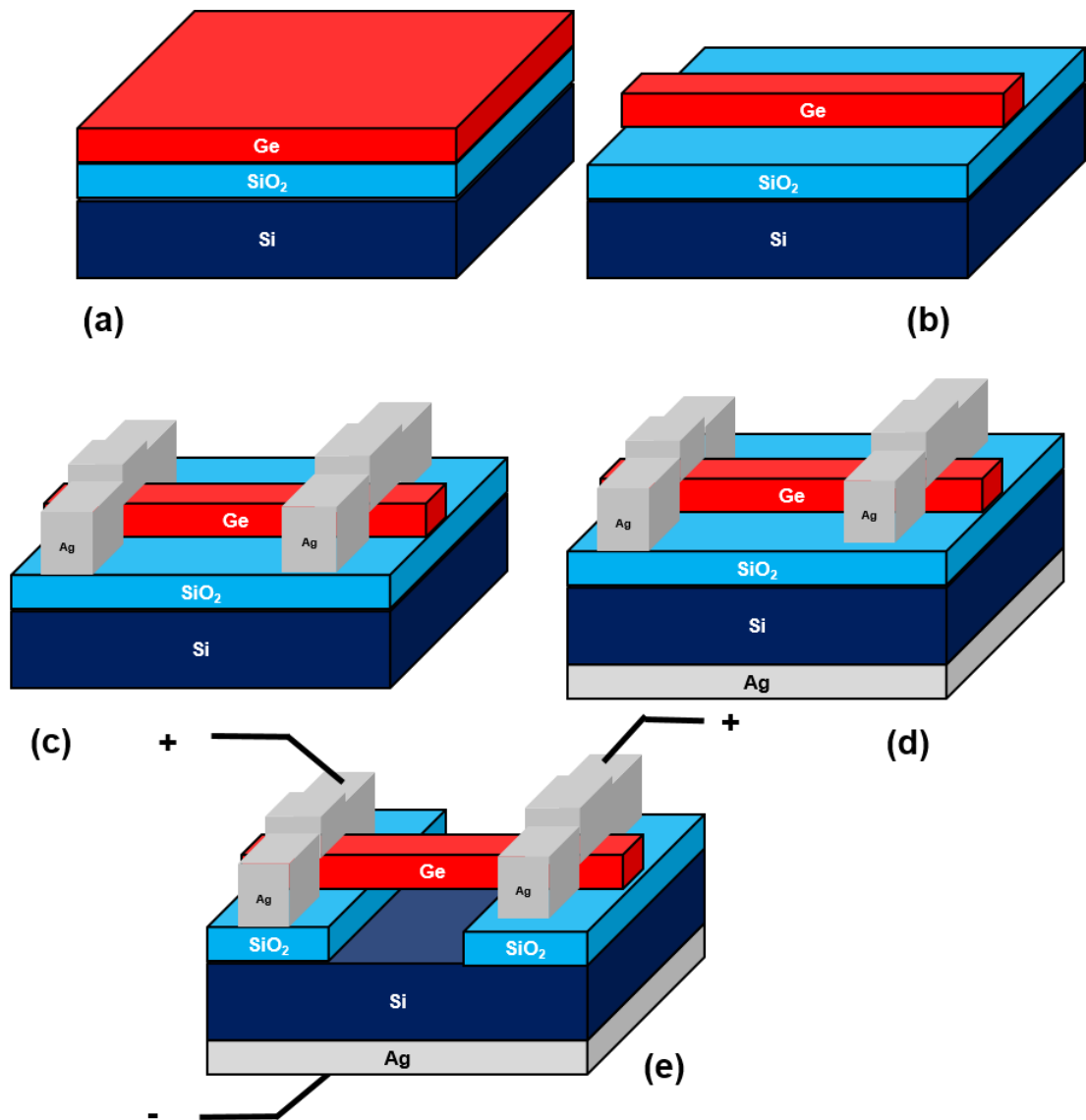
Figure 7.1. The process steps to fabricate the structure to electrostatically actuate Ge nanobeam. (a) GOI structure, (b) the stripe shape obtained after reactive-ion etching, (c) the Ge stripe on insulator with front contacts, (d) the Ge stripe with both contacts, (e) suspended Ge nanobeam with both contacts.

Photoluminescence and electroluminescence measurements of the fabricated structure can also be made to prove light emission enhancement with possible μ-Raman mapping, aiming to show the strain profile.

The actuator introduced in this thesis can potentially serve as the key missing component of a post-fabrication-tunable monolithically-integrated on-chip IR laser and demonstration of on-chip optical communications.

REFERENCES

[1]   G. Moore, "Cramming more components onto integrated circuits," *Electron. Mag.*, vol. 38, no. 8, p. 114, 1965.

[2]   G. E. Moore, "Progress in digital integrated electronics," in *Electron Devices Meeting*, 1975, vol. 21, pp. 11–13.

[3]   T. N. Theis and H.-S. P. Wong, "The end of moore's law: A new beginning for information technology," *Comput. Sci. Eng.*, vol. 19, no. 2, pp. 41–50, 2017.

[4]   M. M. Waldrop, "The chips are down for Moore's law," *Nat. News*, vol. 530, no. 7589, p. 144, 2016.

[5]   J. M. Shalf and R. Leland, "Computing beyond moore's law," *Computer (Long. Beach. Calif).*, vol. 48, no. 12, pp. 14–23, 2015.

[6]   C. Batten, A. Joshi, J. Orcutt, A. Khilo, B. Moss, C. W. Holzwarth, M. A. Popovic, H. Li, H. I. Smith, J. L. Hoyt, F. X. Kartner, R. J. Ram, V. Stojanovic, and K. Asanovic, "Building Many-Core Processor-to-DRAM Networks with Monolithic CMOS Silicon Photonics," *IEEE Micro*, vol. 29, no. 4, pp. 8–21, 2009.

[7]   D. T. and A. Z. and J. E. B. and T. K. and G. T. R. and L. V. and D. M.-M. and E. C. and L. V. and J.-M. F. and J.-M. H. and J. H. S. and D.-X. X. and F. B. and P. O. and G. Z. M. and M. Nedeljkovic, "Roadmap on silicon photonics," *J. Opt.*, vol. 18, no. 7, p. 73003, 2016.

[8]   R. Soref, "The Past, Present, and Future of Silicon Photonics," *IEEE J. Sel. Top. Quantum Electron.*, vol. 12, no. 6, pp. 1678–1687, 2006.

[9]   K. Wen, S. Rumley, P. Samadi, C. P. Chen, and K. Bergman, "Silicon photonics in post Moore's Law era: technological and architectural implications," in *Post-Moore's Era Supercomputing (PMES) Workshop, Salt Lake City. IEEE*, 2016.

[10]   E. E. Haller, "Germanium: From its discovery to SiGe devices," *Mater. Sci. Semicond. Process.*, vol. 9, no. 4–5, pp. 408–422, 2006.

[11]   B. Halford, "Germanium," *Chem. Eng. news*, vol. 81, no. 36, p. 90, 2003.

[12]   C. Claeys and E. Simoen, *Germanium-based technologies: from materials to devices*. elsevier, 2011.

[13]   M. J. H. van Dal, G. Vellianitis, G. Doornbos, B. Duriez, T. M. Shen, C. C. Wu, R. Oxland, K. Bhuwalka, M. Holland, T. L. Lee, C. Wann, C. H. Hsieh, B. H. Lee, K. M. Yin, Z. Q. Wu, M. Passlack, and C. H. Diaz, "Demonstration of scaled Ge p-channel FinFETs integrated on Si," in *2012 International*

Electron Devices Meeting, 2012, p. 23.5.1-23.5.4.

[14]   J. Michel, J. Liu, and L. C. Kimerling, "High-performance Ge-on-Si photodetectors," *Nat. Photonics*, vol. 4, no. 8, p. 527, 2010.

[15]   L. Colace, G. Masini, G. Assanto, H.-C. Luan, K. Wada, and L. C. Kimerling, "Efficient high-speed near-infrared Ge photodetectors integrated on Si substrates," *Appl. Phys. Lett.*, vol. 76, no. 10, pp. 1231–1233, 2000.

[16]   J. Liu, "Monolithically Integrated Ge-on-Si Active Photonics," *Photonics* , vol. 1, no. 3. 2014.

[17]   Y.-H. Kuo, Y. K. Lee, Y. Ge, S. Ren, J. E. Roth, T. I. Kamins, D. A. B. Miller, and J. S. Harris, "Strong quantum-confined Stark effect in germanium quantum-well structures on silicon," *Nature*, vol. 437, no. 7063, p. 1334, 2005.

[18]   A. Frova and P. Handler, "Franz-Keldysh effect in the space-charge region of a germanium p− n junction," *Phys. Rev.*, vol. 137, no. 6A, p. A1857, 1965.

[19]   J. Liu, M. Beals, A. Pomerene, S. Bernardis, R. Sun, J. Cheng, L. C. Kimerling, and J. Michel, "Waveguide-integrated, ultralow-energy GeSi electro-absorption modulators," *Nat. Photonics*, vol. 2, p. 433, May 2008.

[20]   A. E.-J. Lim, T.-Y. Liow, F. Qing, N. Duan, L. Ding, M. Yu, G.-Q. Lo, and D.-L. Kwong, "Novel evanescent-coupled germanium electro-absorption modulator featuring monolithic integration with germanium p-i-n photodetector," *Opt. Express*, vol. 19, no. 6, pp. 5040–5046, 2011.

[21]   J. E. Roth, O. Fidaner, R. K. Schaevitz, Y.-H. Kuo, T. I. Kamins, J. S. Harris, and D. A. B. Miller, "Optical modulator on silicon employing germanium quantum wells," *Opt. Express*, vol. 15, no. 9, pp. 5851–5859, 2007.

[22]   P. Chaisakul, D. Marris-Morini, M.-S. Rouifed, G. Isella, D. Chrastina, J. Frigerio, X. Le Roux, S. Edmond, J.-R. Coudevylle, and L. Vivien, "23 GHz Ge/SiGe multiple quantum well electro-absorption modulator," *Opt. Express*, vol. 20, no. 3, pp. 3219–3224, 2012.

[23]   O. Aldaghri, Z. Ikonić, and R. W. Kelsall, "Optimum strain configurations for carrier injection in near infrared Ge lasers," *J. Appl. Phys.*, vol. 111, no. 5, p. 53106, 2012.

[24]   Y. Ishikawa, K. Wada, D. D. Cannon, J. Liu, H.-C. Luan, and L. C. Kimerling, "Strain-induced band gap shrinkage in Ge grown on Si substrate," *Appl. Phys. Lett.*, vol. 82, no. 13, pp. 2044–2046, 2003.

[25]   J. Liu, X. Sun, D. Pan, X. Wang, L. C. Kimerling, T. L. Koch, and J. Michel, "Tensile-strained, n-type Ge as a gain medium for monolithic laser integration on Si," *Opt. Express*, vol. 15, no. 18, p. 11272, Sep. 2007.

[26] Y. Huo, H. Lin, R. Chen, M. Makarova, Y. Rong, M. Li, T. I. Kamins, J. Vuckovic, and J. S. Harris, "Strong enhancement of direct transition photoluminescence with highly tensile-strained Ge grown by molecular beam epitaxy," *Appl. Phys. Lett.*, vol. 98, no. 1, p. 011111, Jan. 2011.

[27] J. Greil, A. Lugstein, C. Zeiner, G. Strasser, and E. Bertagnolli, "Tuning the Electro-optical Properties of Germanium Nanowires by Tensile Strain," *Nano Lett.*, vol. 12, no. 12, pp. 6230–6234, Dec. 2012.

[28] J. R. Sánchez-Pérez, C. Boztug, F. Chen, F. F. Sudradjat, D. M. Paskiewicz, R. B. Jacobson, M. G. Lagally, and R. Paiella, "Direct-bandgap light-emitting germanium in tensilely strained nanomembranes.," *Proc. Natl. Acad. Sci. U. S. A.*, vol. 108, no. 47, pp. 18893–8, Nov. 2011.

[29] G. Capellini, G. Kozlowski, Y. Yamamoto, M. Lisker, C. Wenger, G. Niu, P. Zaumseil, B. Tillack, A. Ghrib, M. de Kersauson, M. El Kurdi, P. Boucaud, and T. Schroeder, "Strain analysis in SiN/Ge microstructures obtained via Si-complementary metal oxide semiconductor compatible approach," *J. Appl. Phys.*, vol. 113, no. 1, p. 013513, Jan. 2013.

[30] R. W. Millar, K. Gallacher, J. Frigerio, A. Ballabio, A. Bashir, I. MacLaren, G. Isella, and D. J. Paul, "Analysis of Ge micro-cavities with in-plane tensile strains above 2 %," *Opt. Express*, vol. 24, no. 5, p. 4365, Mar. 2016.

[31] M. De Kersauson, M. El Kurdi, S. David, X. Checoury, G. Fishman, S. Sauvage, R. Jakomin, G. Beaudoin, I. Sagnes, and P. Boucaud, "Optical gain in single tensile-strained germanium photonic wire," *Opt. Express*, vol. 19, no. 19, pp. 17925–17934, 2011.

[32] G. Capellini, C. Reich, S. Guha, Y. Yamamoto, M. Lisker, M. Virgilio, A. Ghrib, M. El Kurdi, P. Boucaud, and B. Tillack, "Tensile Ge microstructures for lasing fabricated by means of a silicon complementary metal-oxide-semiconductor process," *Opt. Express*, vol. 22, no. 1, pp. 399–410, 2014.

[33] A. Ghrib, M. El Kurdi, M. de Kersauson, M. Prost, S. Sauvage, X. Checoury, G. Beaudoin, I. Sagnes, and P. Boucaud, "Tensile-strained germanium microdisks," *Appl. Phys. Lett.*, vol. 102, no. 22, p. 221112, Jun. 2013.

[34] A. Ghrib, M. El Kurdi, M. Prost, S. Sauvage, X. Checoury, G. Beaudoin, M. Chaigneau, R. Ossikovski, I. Sagnes, and P. Boucaud, "All-Around SiN Stressor for High and Homogeneous Tensile Strain in Germanium Microdisk Cavities," *Adv. Opt. Mater.*, vol. 3, no. 3, pp. 353–358, Mar. 2015.

[35] M. J. Süess, R. Geiger, R. A. Minamisawa, G. Schiefler, J. Frigerio, D. Chrastina, G. Isella, R. Spolenak, J. Faist, and H. Sigg, "Analysis of enhanced light emission from highly strained germanium microbridges," *Nat. Photonics*, vol. 7, p. 466, Apr. 2013.

[36] D. S. Sukhdeo, D. Nam, J.-H. Kang, M. L. Brongersma, and K. C. Saraswat, "Direct bandgap germanium-on-silicon inferred from 5.7% <100>; uniaxial tensile strain [Invited]," *Photonics Res.*, vol. 2, no. 3, pp. A8–A13, 2014.

[37] S. Bao, D. Kim, C. Onwukaeme, S. Gupta, K. Saraswat, K. H. Lee, Y. Kim, D. Min, Y. Jung, H. Qiu, H. Wang, E. A. Fitzgerald, C. S. Tan, and D. Nam, "Low-threshold optically pumped lasing in highly strained germanium nanowires," *Nat. Commun.*, vol. 8, no. 1, p. 1845, Dec. 2017.

[38] D. Nam, D. S. Sukhdeo, J.-H. Kang, J. Petykiewicz, J. H. Lee, W. S. Jung, J. Vučković, M. L. Brongersma, and K. C. Saraswat, "Strain-Induced Pseudoheterostructure Nanowires Confining Carriers at Room Temperature with Nanoscale-Tunable Band Profiles," *Nano Lett.*, vol. 13, no. 7, pp. 3118–3123, Jul. 2013.

[39] Y. Zhou, J. Sun, J. Jiang, R. Zhang, J. Gao, and H. Zhou, "Analysis of light emission performance of pseudoheterostructure diode based on germanium micro-bridge," *Opt. Commun.*, vol. 397, pp. 153–160, 2017.

[40] J. Liu, X. Sun, L. C. Kimerling, and J. Michel, "Direct-gap optical gain of Ge on Si at room temperature," *Opt. Lett.*, vol. 34, no. 11, pp. 1738–1740, 2009.

[41] R. E. Camacho-Aguilera, Y. Cai, N. Patel, J. T. Bessette, M. Romagnoli, L. C. Kimerling, and J. Michel, "An electrically pumped germanium laser," *Opt. Express*, vol. 20, no. 10, p. 11316, May 2012.

[42] L. Carroll, P. Friedli, S. Neuenschwander, H. Sigg, S. Cecchi, F. Isa, D. Chrastina, G. Isella, Y. Fedoryshyn, and J. Faist, "Direct-gap gain and optical absorption in germanium correlated to the density of photoexcited carriers, doping, and strain," *Phys. Rev. Lett.*, vol. 109, no. 5, p. 57402, 2012.

[43] G. Scappucci, G. Capellini, W. M. Klesse, and M. Y. Simmons, "New avenues to an old material: controlled nanoscale doping of germanium," *Nanoscale*, vol. 5, no. 7, pp. 2600–2615, 2013.

[44] W.-J. Yin, X.-G. Gong, and S.-H. Wei, "Origin of the unusually large band-gap bowing and the breakdown of the band-edge distribution rule in the Sn x Ge 1− x alloys," *Phys. Rev. B*, vol. 78, no. 16, p. 161203, 2008.

[45] S. Gupta, B. Magyari-Köpe, Y. Nishi, and K. C. Saraswat, "Achieving direct band gap in germanium through integration of Sn alloying and external strain," *J. Appl. Phys.*, vol. 113, no. 7, p. 73707, 2013.

[46] F. A. Trumbore, "Solid solubilities and electrical properties of tin in germanium single crystals," *J. Electrochem. Soc.*, vol. 103, no. 11, pp. 597–600, 1956.

[47] J. Kouvetakis, J. Menendez, and A. V. G. Chizmeshya, "Tin-based group IV semiconductors: New platforms for opto-and microelectronics on silicon,"

Annu. Rev. Mater. Res., vol. 36, pp. 497–554, 2006.

[48]   J. Taraci, J. Tolle, J. Kouvetakis, M. R. McCartney, D. J. Smith, J. Menendez, and M. A. Santana, "Simple chemical routes to diamond-cubic germanium–tin alloys," *Appl. Phys. Lett.*, vol. 78, no. 23, pp. 3607–3609, 2001.

[49]   B. Vincent, F. Gencarelli, H. Bender, C. Merckling, B. Douhard, D. H. Petersen, O. Hansen, H. H. Henrichsen, J. Meersschaut, and W. Vandervorst, "Undoped and in-situ B doped GeSn epitaxial growth on Ge by atmospheric pressure-chemical vapor deposition," *Appl. Phys. Lett.*, vol. 99, no. 15, p. 152103, 2011.

[50]   G. Grzybowski, R. T. Beeler, L. Jiang, D. J. Smith, J. Kouvetakis, and J. Menendez, "Next generation of Ge1− y Sn y (y= 0.01-0.09) alloys grown on Si (100) via Ge3H8 and SnD4: Reaction kinetics and tunable emission," *Appl. Phys. Lett.*, vol. 101, no. 7, p. 72105, 2012.

[51]   S. A. Ghetmiri, W. Du, J. Margetis, A. Mosleh, L. Cousar, B. R. Conley, L. Domulevicz, A. Nazzal, G. Sun, and R. A. Soref, "Direct-bandgap GeSn grown on silicon with 2230 nm photoluminescence," *Appl. Phys. Lett.*, vol. 105, no. 15, p. 151109, 2014.

[52]   J. Mathews, R. T. Beeler, J. Tolle, C. Xu, R. Roucka, J. Kouvetakis, and J. Menéndez, "Direct-gap photoluminescence with tunable emission wavelength in Ge 1− y Sn y alloys on silicon," *Appl. Phys. Lett.*, vol. 97, no. 22, p. 221912, 2010.

[53]   R. Roucka, J. Mathews, R. T. Beeler, J. Tolle, J. Kouvetakis, and J. Menéndez, "Direct gap electroluminescence from Si/Ge 1− y Sn yp-i-n heterostructure diodes," *Appl. Phys. Lett.*, vol. 98, no. 6, p. 61109, 2011.

[54]   S. Wirths, Z. Ikonic, A. T. Tiedemann, B. Holländer, T. Stoica, G. Mussler, U. Breuer, J. M. Hartmann, A. Benedetti, and S. Chiussi, "Tensely strained GeSn alloys as optical gain media," *Appl. Phys. Lett.*, vol. 103, no. 19, p. 192110, 2013.

[55]   S. Wirths, R. Geiger, N. von den Driesch, G. Mussler, T. Stoica, S. Mantl, Z. Ikonic, M. Luysberg, S. Chiussi, J. M. Hartmann, H. Sigg, J. Faist, D. Buca, and D. Grützmacher, "Lasing in direct-bandgap GeSn alloy grown on Si," *Nat. Photonics*, vol. 9, no. 2, pp. 88–92, Feb. 2015.

[56]   S. Al-Kabi, S. A. Ghetmiri, J. Margetis, T. Pham, Y. Zhou, W. Dou, B. Collier, R. Quinde, W. Du, A. Mosleh, J. Liu, G. Sun, R. A. Soref, J. Tolle, B. Li, M. Mortazavi, H. A. Naseem, and S.-Q. Yu, "An optically pumped 2.5 μm GeSn laser on Si operating at 110 K," *Appl. Phys. Lett.*, vol. 109, no. 17, p. 171105, Oct. 2016.

[57]   V. Reboud, A. Gassenq, N. Pauc, J. Aubin, L. Milord, Q. M. Thai, M.

Bertrand, K. Guilloy, D. Rouchon, and J. Rothman, "Optically pumped GeSn micro-disks with 16% Sn lasing at 3.1 μ m up to 180 K," *Appl. Phys. Lett.*, vol. 111, no. 9, p. 92101, 2017.

[58]   D. Stange, S. Wirths, R. Geiger, C. Schulte-Braucks, B. Marzban, N. von den Driesch, G. Mussler, T. Zabel, T. Stoica, J.-M. Hartmann, S. Mantl, Z. Ikonic, D. Grützmacher, H. Sigg, J. Witzens, and D. Buca, "Optically Pumped GeSn Microdisk Lasers on Si," *ACS Photonics*, vol. 3, no. 7, pp. 1279–1285, Jul. 2016.

[59]   R. W. Millar, D. C. S. Dumas, K. Gallacher, P. Jahandar, M. Myronov, and D. J. Paul, "Tensile strained GeSn mid-infrared light emitters," in *Group IV Photonics (GFP), 2017 IEEE 14th International Conference on*, 2017, pp. 49–50.

[60]   C. Liu, *Foundations of MEMS*. Pearson Education India, 2012.

[61]   J. A. Kubby, *A Guide to Hands-on MEMS Design and Prototyping*. Cambridge: Cambridge University Press, 2011.

[62]   M. Tilli, M. Paulasto-Krockel, V. M. Airaksinen, S. Franssila, V. Lindroos, A. Lehto, and T. Motooka, *Handbook of Silicon Based MEMS Materials and Technologies*. Elsevier Science, 2009.

[63]   E. Chan and R. W. Dutton, *Electrostatic micromechanical actuator with extended range of travel*, vol. 9. 2000.

[64]   E. S. Hung and S. D. Senturia, *Extending the travel range of analog-tuned electrostatic actuators*, vol. 8. 2000.

[65]   J. Zou, C. Liu, and J. Schutt-Aine, *Development of a Wide-Tuning-Range Two-Parallel-Plate Tunable Capacitor for Integrated Wireless Communication Systems*, vol. 11. 2001.

[66]   R. Nadal-Guardia, A. Dehe, R. Aigner, and L. M. Castaner, "Current drive methods to extend the range of travel of electrostatic microactuators beyond the voltage pull-in point," *J. Microelectromechanical Syst.*, vol. 11, no. 3, pp. 255–263, Jun. 2002.

[67]   S. Chowdhury, M. Ahmadi, and W. C. Miller, "Pull-in voltage study of electrostatically actuated fixed-fixed beams using a VLSI on-chip interconnect capacitance model," *J. Microelectromechanical Syst.*, vol. 15, no. 3, pp. 639–651, 2006.

[68]   B. C. and E. G. Lovell, "Improved analysis of microbeams under mechanical and electrostatic loads," *J. Micromechanics Microengineering*, vol. 7, no. 1, p. 24, 1997.

[69]   M. H. Miller, J. A. Perrault, G. G. Parker, B. P. Bettig, and T. G. Bifano,

"Simple models for piston-type micromirror behavior," *J. Micromechanics Microengineering*, vol. 16, no. 2, p. 303, 2006.

[70] S. Pamidighantam, R. Puers, K. Baert, and H. A. C. Tilmans, "Pull-in voltage analysis of electrostatically actuated beam structures with fixed–fixed and fixed–free end conditions," *J. Micromechanics Microengineering*, vol. 12, no. 4, p. 458, 2002.

[71] J. Zhang and Y. Fu, "Pull-in analysis of electrically actuated viscoelastic microbeams based on a modified couple stress theory," *Meccanica*, vol. 47, no. 7, pp. 1649–1658, Oct. 2012.

[72] H. A. C. Tilmans and R. Legtenberg, "Electrostatically driven vacuum-encapsulated polysilicon resonators: Part II. Theory and performance," *Sensors Actuators A Phys.*, vol. 45, no. 1, pp. 67–84, 1994.

[73] A. F. Bower, *Applied mechanics of solids*. CRC press, 2009.

[74] V. Nishawala, "A study of large deflection of beams and plates." Rutgers University-Graduate School-New Brunswick, 2011.

[75] Q. Zhang, Y. Liu, J. Yan, C. Zhang, Y. Hao, and G. Han, "Theoretical investigation of tensile strained GeSn waveguide with Si 3 N 4 liner stressor for mid-infrared detector and modulator applications," *Opt. Express*, vol. 23, no. 6, pp. 7924–7932, 2015.

[76] J. S. Townsend, *Electricity in gases*. Рипол Классик, 1915.

[77] E. Husain and R. S. Nema, "Analysis of Paschen Curves for air, N2 and SF6 Using the Townsend Breakdown Equation," *IEEE Trans. Electr. Insul.*, vol. EI-17, no. 4, pp. 350–353, 1982.

[78] P. A. Tipler and J. R. Meyer-Arendt, "College physics," *Appl. Opt.*, vol. 26, p. 5220, 1987.

[79] R.-T. Lee, H.-H. Chung, and Y.-C. Chiou, "Arc erosion behaviour of silver electric contacts in a single arc discharge across a static gap," *IEE Proceedings-Science, Meas. Technol.*, vol. 148, no. 1, pp. 8–14, 2001.

[80] Y. Hirata, K. Ozaki, U. Ikeda, and M. Mizoshiri, "Field emission current and vacuum breakdown by a pointed cathode," *Thin Solid Films*, vol. 515, no. 9, pp. 4247–4250, 2007.

[81] P. Kisliuk, "Electron emission at high fields due to positive ions," *J. Appl. Phys.*, vol. 30, no. 1, pp. 51–55, 1959.

[82] R. S. Dhariwal, J.-M. Torres, and M. P. Y. Desmulliez, "Electric field breakdown at micrometre separations in air and nitrogen at atmospheric pressure," *IEE Proceedings-Science, Meas. Technol.*, vol. 147, no. 5, pp. 261–

265, 2000.

[83]   W. Zhang, T. S. Fisher, and S. V Garimella, "Simulation of ion generation and breakdown in atmospheric air," *J. Appl. Phys.*, vol. 96, no. 11, pp. 6066–6072, 2004.

[84]   M. Radmilović-Radjenović, J. K. Lee, F. Iza, and G. Y. Park, "Particle-in-cell simulation of gas breakdown in microgaps," *J. Phys. D. Appl. Phys.*, vol. 38, no. 6, p. 950, 2005.

[85]   A. Semnani, A. Venkattraman, A. A. Alexeenko, and D. Peroulis, "Pre-breakdown evaluation of gas discharge mechanisms in microgaps," *Appl. Phys. Lett.*, vol. 102, no. 17, p. 174102, 2013.

[86]   P. G. Slade and E. D. Taylor, "Electrical breakdown in atmospheric air between closely spaced (0.2/spl mu/m-40/spl mu/m) electrical contacts," *IEEE Trans. components Packag. Technol.*, vol. 25, no. 3, pp. 390–396, 2002.

[87]   A. Peschot, C. Poulain, N. Bonifaci, and O. Lesaint, "Electrical breakdown voltage in micro-and submicrometer contact gaps (100nm-10μm) in air and nitrogen," in *Electrical Contacts (Holm), 2015 IEEE 61st Holm Conference on*, 2015, pp. 280–286.

[88]   D. Lyon and A. Hubler, "Gap size dependence of the dielectric strength in nano vacuum gaps," *IEEE Trans. Dielectr. Electr. Insul.*, vol. 20, no. 4, pp. 1467–1471, 2013.

[89]   J. W. McPherson, "Determination of the nature of molecular bonding in silica from time-dependent dielectric breakdown data," *J. Appl. Phys.*, vol. 95, no. 12, pp. 8101–8109, 2004.

[90]   J. W. McPherson, J. Kim, A. Shanware, H. Mogul, and J. Rodriguez, "Trends in the ultimate breakdown strength of high dielectric-constant materials," *IEEE Trans. Electron Devices*, vol. 50, no. 8, pp. 1771–1778, 2003.

[91]   N. H. Macmillan, "The theoretical strength of solids," *J. Mater. Sci.*, vol. 7, no. 2, pp. 239–254, 1972.

[92]   S. Hoffmann, I. Utke, B. Moser, J. Michler, S. H. Christiansen, V. Schmidt, S. Senz, P. Werner, U. Gösele, and C. Ballif, "Measurement of the bending strength of vapor− liquid− solid grown silicon nanowires," *Nano Lett.*, vol. 6, no. 4, pp. 622–625, 2006.

[93]   D. A. Smith, V. C. Holmberg, and B. A. Korgel, "Flexible Germanium Nanowires: Ideal Strength, Room Temperature Plasticity, and Bendable Semiconductor Fabric," *ACS Nano*, vol. 4, no. 4, pp. 2356–2362, Apr. 2010.

[94]   M. Balseanu, L.-Q. Xia, V. Zubkov, M. Le, J. Lee, and H. M'Saad, "Stress Modulation of PECVD Silicon Nitride," in *Meeting Abstracts*, 2006, no. 13, p.

532.

[95] M. Balseanu, M. S. Cox, L.-Q. Xia, M.-Y. Shek, J. Lee, V. Zubkov, T.-F. Huang, R. Wang, I. Roflox, and H. M'saad, "Method to increase tensile stress of silicon nitride films using a post PECVD deposition UV cure." Google Patents, 06-Mar-2012.

[96] A. Gassenq, K. Guilloy, G. Osvaldo Dias, N. Pauc, D. Rouchon, J.-M. Hartmann, J. Widiez, S. Tardif, F. Rieutord, J. Escalante, I. Duchemin, Y.-M. Niquet, R. Geiger, T. Zabel, H. Sigg, J. Faist, A. Chelnokov, V. Reboud, and V. Calvo, "1.9% bi-axial tensile strain in thick germanium suspended membranes fabricated in optical germanium-on-insulator substrates for laser applications," *Appl. Phys. Lett.*, vol. 107, no. 19, p. 191904, Nov. 2015.

[97] B. Dutt, D. S. Sukhdeo, D. Nam, B. M. Vulovic, Z. Yuan, and K. C. Saraswat, "Roadmap to an efficient germanium-on-silicon laser: strain vs. n-type doping," *IEEE Photonics J.*, vol. 4, no. 5, pp. 2002–2009, 2012.